2010

Magnetic surface nanostructures

Axel Enders
University of Nebraska at Lincoln, a.enders@me.com

Ralph A. Skomski
University of Nebraska-Lincoln, rskomski2@unl.edu

Jan Honolka
Max-Planck-Institut für Festkörperforschung, honolka@fzu.cz

J. Phys.: Condens. Matter **22** (2010) 433001 (32pp) doi:10.1088/0953-8984/22/43/433001

TOPICAL REVIEW

Magnetic surface nanostructures

A Enders[1], R Skomski[1] and J Honolka[2]

[1] Department of Physics and Astronomy and Nebraska Center for Materials and Nanoscience, University of Nebraska, Lincoln, NE 68588, USA
[2] Max Planck Institute for Solid State Research, Heisenbergstrasse 1, D-70569 Stuttgart, Germany

E-mail: aenders2@unl.edu

Received 11 June 2010, in final form 6 September 2010
Published 7 October 2010
Online at stacks.iop.org/JPhysCM/22/433001

Abstract
Recent trends in the emerging field of surface-supported magnetic nanostructures are reviewed. Current strategies for nanostructure synthesis are summarized, followed by a predominantly theoretical description of magnetic phenomena in surface magnetic structures and a review of experimental research in this field. Emphasis is on Fe- or Co-based nanostructures in various low-dimensional geometries, which are studied as model systems to explore the effects of dimensionality, atomic coordination, chemical bonds, alloying and, most importantly, interactions with the supporting substrate on the magnetism. This review also includes a discussion of closely related systems, such as 3d element impurities integrated into organic networks, surface-supported Fe-based molecular magnets, Kondo systems or 4d element nanostructures that exhibit emergent magnetism, thereby bridging the traditional areas of surface science, molecular physics and nanomagnetism.

(Some figures in this article are in colour only in the electronic version)

Contents

1. Introduction

The ongoing race to achieve a performance increase of devices and materials has stimulated tremendous research efforts on nanomaterials, to understand, improve and exploit their physical and chemical properties. With regard to magnetism, nanostructures with controlled properties are urgently needed to further advance devices for information processing and storage, energy applications, catalysis and permanent magnets [1–5]. Progress in materials synthesis has recently led to new types of nanostructures whose behavior is often very different from that of bulk and thin-film structures, or reveals completely new aspects of known phenomena. The fabrication of simple magnetic structures,

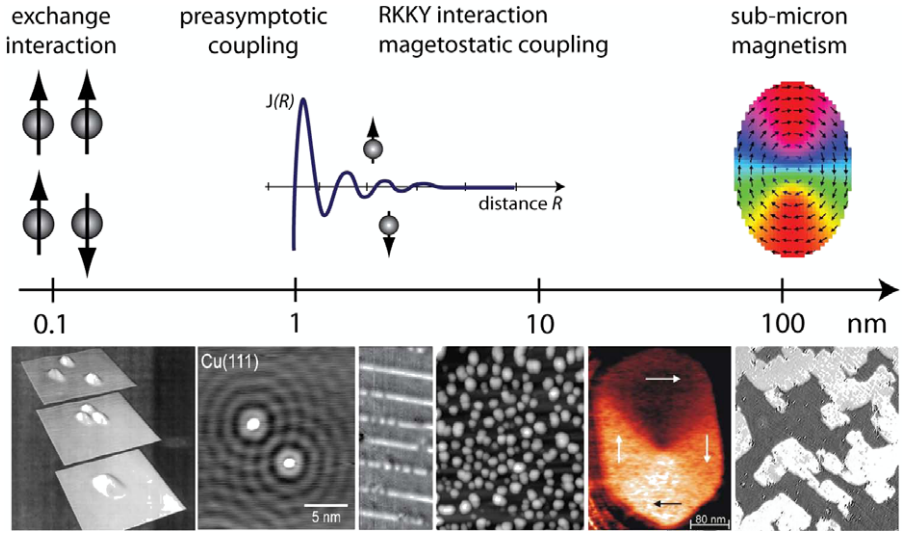

Figure 1. Relevant length scales in magnetism. Exchange interaction is essentially an atomic phenomenon, with relevant length scales of a few ångströms. RKKY and magnetostatic interactions can extend over several tens of nm. Bottom: examples of structures, displaying characteristic phenomena as above: spin frustration in Cr trimers [6], Friedel oscillations in Cu(111) around Co adatoms [7], chains of Fe atoms on Pt(997) [8], Fe clusters on Pt(111) [9], magnetic vortex in an Fe island [10] and magnetic domains in 3 ML Fe/Cu(100) [11] (from left).

such as free clusters and nanoparticles, core–shell structures, granular bulk materials, nanowires, thin-film and multilayer structures, and nanotubes is possible with current synthesis strategies [12]. Such structures are valuable model systems for the study of fundamental magnetic phenomena. But also more complex nanostructures are now possible on metallic substrates by exploiting template effects or by using advanced deposition or self-assembly techniques [13–16]. A recent trend is the synthesis of hybrid materials, such as magnetic metals in contact with organics or oxides. The substrate or the embedding matrix often influences the properties of the structures they support and can thus be exploited to modify, enhance or suppress selected properties.

The focus of this review is on the emerging field of such magnetic surface nanostructures. Their physics derives from the interaction of the laterally constrained nanostructural units with the substrate. This distinguishes the present structures from extended two-dimensional structures, such as thin films and multilayers, and from traditional nanostructures such as nanotubes, nanoparticles and nanocomposites. Some currently studied phenomena are the anisotropy and Kondo physics of impurities, non-collinear spin structures caused by Dzyaloshinskii–Moriya interactions, magnetic frustration in Cr trimers, ligand field effects in organic networks, molecular magnetism, magnetism in surface alloys and emergent 4d/5d element magnetism. We review current synthesis strategies and magnetic properties of magnetic surface nanostructures, with particular emphasis on self-assembled magnetic Fe and Co nanostructures on metallic surfaces. Emphasis is on structures of intermediate size, between atomic-scale magnetism on a length scale of a few ångströms (1 Å = 0.1 nm) and magnetism in structures of about 10 nm in size (figure 1).

Much of the new physics in surface nanostructures derives from interactions with the supporting substrate. Their magnetism is also affected by the internal dimensionality, atomic coordination, chemical bonding and alloying. From a fundamental point of view, interactions in magnetic surface nanostructures are similar to interactions in other low-dimensional magnets and nanostructures. A quantum-mechanical mean-field expression for the onset of ferromagnetism in transition metals is the Stoner criterion $I \cdot D(E_F) > 1$ [17]. Here, I is an interatomic Coulomb integral and $D(E_F)$ is the density of states (DOS) at the Fermi level, which is roughly proportional to the inverse bandwidth, $1/W$. This equation can also be used for nanostructures if one replaces the *total* density of states by the *local* density of states. Typically, the Stoner integral I is of the order of 1 eV for transition metals [18], but the DOS strongly depends on the local atomic environment. This creates [19–21], enhances [22–24] or reduces [25] the magnetization and yields phenomena such as high-spin–low-spin transitions [26]. In some cases, the coupling is antiferromagnetic, especially if the structures contain atoms from the middle of the transition-metal series, such as Mn. The local DOS roughly scales as $1/\sqrt{z}$, where z is the number of nearest neighbors, so that surfaces, magnetic molecules and small-scale nanostructures tend to exhibit a more pronounced trend towards ordered spin alignment (ferromagnetic or antiferromagnetic) than bulk materials. This phenomenon is sometimes referred to as emergent magnetism. Strongly exchange-enhanced Pauli paramagnets such as Pd, Rh and Pt nearly satisfy the Stoner criterion and get spin-polarized by neighboring Fe or Co atoms or in certain atomic environments.

The origin of the Stoner criterion is the Pauli principle, which forbids the occupancy of a given orbital by two electrons of parallel spin (↑↑). Such electrons stay away from each other, thereby reducing their Coulomb energy and producing a ferromagnetic spin alignment. Another consequence of the Pauli principle is *interatomic exchange*, which yields

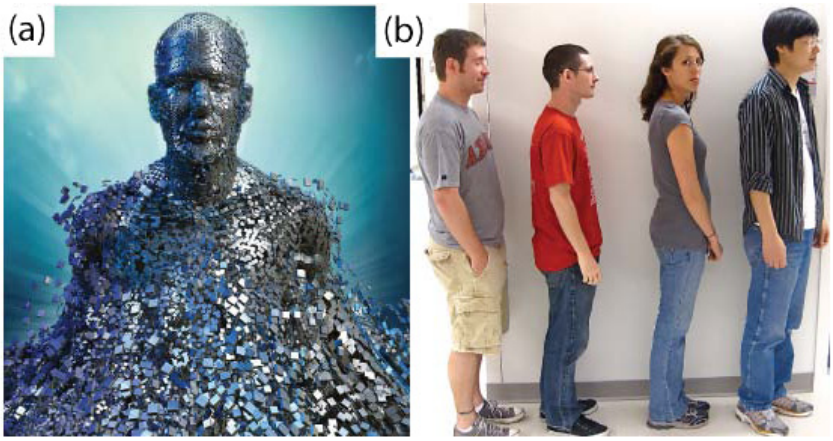

Figure 2. Commonly, a distinction is made between *self-assembly* (a) and *self-organization* (b). Self-assembly refers to the spontaneous formation of structures from individual building blocks, such as atoms or molecules, in solution or at surfaces. The emergence of the T-1000 Terminator from liquid in the movie 'Terminator 2: Judgment Day' is an example of self-assembly. (Source: New Scientist magazine. Reprint with permission.) Self-organization, not further discussed in this review, refers to the formation of larger, ordered assemblies from rather complex entities. An example is a queue of students outside the lecture hall.

a ferromagnetic (FM) or antiferromagnetic (AFM) coupling between neighboring atomic moments. It is realized in many forms, such as direct exchange, long-range oscillating Ruderman–Kittel (RKKY) exchange mediated by conduction electrons, indirect exchange mediated by main-group elements, Stoner-like preasymptotic ferromagnetic exchange [27] and double exchange involving charge fluctuations. Exchange interactions typically dominate on a length scale of a few interatomic distances and yield or affect a broad variety of phenomena, including FM–AFM transitions [28], spiral and other non-collinear spin structures, magnetic vortices and magnetic domains, and domain walls (figure 1).

A second class of important interactions is relativistic rather than exclusively electrostatic and yields a variety of effects, such as orbital moment, spin–orbit coupling, magnetic anisotropy, Dresselhaus and Rashba terms in two and three dimensions, respectively, and Dzyaloshinskii–Moriya exchange. Relativistic effects increase with the velocity of the electrons, so that heavy elements such as Pd and Pt often exhibit substantial orbital moments and anisotropies [29, 30, 27]. For example, due to the high spin–orbit coupling, relatively small induced 4d/5d moments translate into large anisotropies. Zeeman and magnetostatic interactions can also be listed here, because their origin is relativistic. Magnetostatic dipole interactions are often unimportant on the atomic scale but tend to dominate the interatomic exchange on sub-micromagnetic length scales larger than a few tens of nm [31].

Recent progress in materials synthesis has made it possible to fabricate nanostructures with atomic or molecular precision. The literature is rich in articles addressing growth phenomena as a function of various parameters, and interested readers can find comprehensive overviews in numerous review articles or books, such as [32–35]. There are two major fabrication strategies, commonly referred to as *top-down* and *bottom-up* designs. The top-down approach achieves structures of the desired shape, composition and functionality by sculpturing bulk materials, partially removing material (cutting, milling, etching) or adding material using methods such as molecular beam epitaxy (MBE) and sputter deposition. An important example in this category is photolithography, which is the method of choice in the semiconductor industry for mass production of semiconductor chips. The minimum feature size that can currently be achieved with this method is approximately 50 nm if deep-ultraviolet light is used.

By contrast, the bottom-up approach starts from atoms, clusters or molecules, which are controlled to create larger structures or assemblies (see figure 2). The most widely used bottom-up approach is self-assembled growth, or self-assembly. It refers to the spontaneous formation of structures from atoms or molecules, in solution or at crystalline surfaces. This yields molecular crystals having sizes of many nanometers or even micrometers, but also extended two-dimensional (2D) layers or networks, alloys, metallo-organic hybrid structures, linear chains and clusters at surfaces. At present, self-assembly is the only method capable of producing structures in the nanometer and sub-nanometer size range.

In this review, we outline the state of the art in the field of magnetic surface nanostructures. Our focus is on artificially structured systems and we do not consider continuous layers or multilayers. Section 2 summarizes fabrication methods. Section 3 is devoted to physical effects commonly found in these structures. Experimental systems that exhibit characteristic nanoscale magnetic features due to, and despite, interactions with the substrate are discussed in section 4 and a tentative outlook to future research is presented in section 5.

2. Synthesis of magnetic nanostructures by self-assembly

In this section, we will summarize relevant strategies for the fabrication of artificial magnetic structures with nearly atomically defined structural properties. A focus is on

structures made of or containing 3d, 4d or 5d metals, but this section is also expanded to include a brief discussion of organic and insulator nanomaterials.

2.1. Nanostructures on flat surfaces

2.1.1. Islands and films. Self-assembly typically occurs during the deposition of building blocks, such as atoms, small clusters or molecules, on surfaces under ultrahigh vacuum conditions. Simple and complex structures emerge due to a multitude of effects, which will be described in this section. In the simplest case of heteroepitaxial growth, metal atoms are deposited on atomically flat, crystalline substrates at a given deposition rate and substrate temperature, to form islands or layers. The growth can be discussed as a wetting problem if it occurs near thermal equilibrium, and structures emerge following energy considerations [36, 37]. In such cases, the specific surface free energies at the interfaces can be used to predict the growth mode of the adlayer, according to

$$\gamma_f + \gamma_i - \gamma_s = \Delta\gamma. \quad (1)$$

The quantities γ_f, γ_i and γ_s are the surface free energies at the film–vacuum interface, the film–substrate interface and the substrate–vacuum interface, respectively.

Despite its simplicity, equation (1) often predicts the growth mode of the adlayer correctly. Layer-by-layer growth, or Frank–van der Merwe growth, is expected if the topmost layer is completely wetting the surface underneath. In metal heteroepitaxy and, as a rough estimate, this is the case if $\gamma_s > \gamma_f$, and if γ_i is sufficiently small, so that $\Delta\gamma < 0$. Examples are the homoepitaxial growth of Pt on Pt(111) [38] and the heteroepitaxy of Fe on Cu(111) during pulsed-laser deposition [39]. In some instances, layer-by-layer growth can be enforced by the use of surfactants. The role of a surfactant, which stays on top of the adlayer during growth, is to lower γ_f or to decrease the energy barriers for diffusion [40].

Island growth, or Volmer–Weber growth, is typically found if the adlayer material does not wet the substrate easily. According to the criterion above, this is expected if $\Delta\gamma > 0$ or if $\gamma_s < \gamma_f$. Examples for island growth are the growth of Co on Cu(111) [41] and the growth of Ag on Pt(111) [42].

Intermediate between layer-by-layer and island growth is the so-called Stranski–Krastanov growth. Here, the adlayer initially grows layer by layer, thus wetting the substrate perfectly. Above a critical thickness though, the growth mode changes and three-dimensional (3D) islands are beginning to form. Stranski–Krastanov growth is observed, for instance, if $\gamma_s \approx \gamma_f$, but also if γ_i changes with increasing film thickness so that $\Delta\gamma < 0$ is no longer fulfilled at higher coverages. Fe on W(110) and W(100) surfaces, for instance, grows in this mode, with critical thicknesses of 1.5 ML and 2 ML, respectively [43–47].

Even though many examples in the literature are consistent with this simple criterion, the correct predictions of the growth mode with equation (1) are often not possible. Known limitations can be summarized as follows: (i) in most cases, the film does not grow near the thermodynamic equilibrium. Such an equilibrium would imply that the flux of impinging atoms is sufficiently low, in fact comparable to the flux of atoms desorbed from the substrate, so that no net growth would actually occur. However, a typical deposition rate of 1 Å min^{-1} corresponds to a particle flux of 10^{13} s^{-1} cm^{-2}, which is six orders of magnitude larger than a flux of 10^{7} s^{-1} cm^{-2}, which would correspond to the vapor pressure of Fe, Ni or Co at 300 K. Therefore, growth phenomena are inherently non-equilibrium processes. The supersaturation, defined as the actual adatom density normalized to the equilibrium adatom density, describes to which extent the evolving structures will be determined by the thermodynamic parameters, or by the growth kinetics [48, 49]. (ii) Values for the surface free energies of bulk materials are often poor estimates for γ_f. The electronic structure of monolayer thin films often deviates from the bulk structure due to the reduced coordination and interactions with the substrates. (iii) The interface energy, γ_i, is often unknown and estimated from simplified models. (iv) Interface mixing, lattice mismatch and structural anisotropies are usually not considered.

For these reasons, film growth is often a non-equilibrium process and, as such, limited by the kinetics of the surface diffusion. Key parameters in the kinetic growth regime are the deposition rate of atoms or molecules, R, and the diffusivity of atoms at the surface, D. The latter is temperature-dependent and determines the average distance an adatom has to travel to nucleate a new aggregate or to attach to an already existing aggregate. If the deposition is slow compared to the diffusivity then the growth takes place closer to equilibrium. If, on the other hand, the deposition is fast, the individual atomistic processes become increasingly important and the growth is essentially determined by kinetics, i.e. thermally activated motion in the presence of diffusion barriers. In particular, the nucleation of aggregates at very low coverages results in the decrease of the mean free path of atoms, which triggers a crossover from a nucleation-dominated regime to an island growth regime. The size and areal density of adlayer islands is dependent on the ratio R/D [50]. As a trend, a large number of small islands is found at low temperature and high deposition rate, while fewer but larger islands are formed at high temperatures or low deposition rates.

Besides the described parameters, D and R, mainly the details of the diffusion of single atoms on surfaces determine the shape and size of emerging metallic structures. Fundamental diffusion processes are diffusion on terraces, over steps, along edges and across corners. Each of these processes is associated with a characteristic energy barrier. The diffusion across such barriers is thermally activated, with the respective rate depending on the barrier height. For a given material system, we have thus a natural hierarchy of relevant diffusion barriers, and the growing aggregates can be shaped by selective activation/freezing of certain diffusion processes via the temperature [49, 51].

One system that exemplifies the importance of the hierarchy of activated motion in the kinetically limited growth is Ag on Pt(111). Ag atoms impinging on the Pt surface diffuse in a random walk, until they attach to the perimeter of a growing aggregate. If more than one diffusion barrier is present after the nucleation regime then the perimeter mobility of the

adatoms is determined by the substrate temperature, while the growth velocity is determined by the flux of the deposition. For a given temperature, an increase in flux can trigger a transition from randomly ramified islands to the growth of symmetrically branched dendritic structures [52]. The balance between diffusion speed and flux of deposition determines therefore the shape of the growing aggregates.

In general, the energy barriers for atomic diffusion depend on the crystalline direction on otherwise flat substrate surfaces. Such substrates make useful natural templates for the growth of one-dimensional systems, which will be discussed in section 2.2. The diffusion speed can, however, also be anisotropic if the barrier heights are identical for diffusion along two perpendicular directions, as has been demonstrated by Reuter *et al* for Fe on W(110) [53]. Here, for an atom to hop into the neighboring site along the ⟨110⟩ direction or the ⟨100⟩ direction requires identical jumps. Yet, the total distance traveled after two such jumps is different along the ⟨100⟩ and ⟨110⟩ directions, resulting in Fe structures elongated in the ⟨110⟩ direction.

These examples show that heteroepitaxial growth, in its simplest form, is useful to fabricate ultrathin films, sandwich layers, superlattices and islands, with good control over structural and interface quality.

2.1.2. Core–shell structures. Two-dimensional core–shell nano-islands can be formed by exploiting simple nucleation and step edge diffusion processes [54]. This approach specifically relies on the change in growth mode from a nucleation regime to an island growth regime as the coverage increases. The island cores are initially formed by deposition on the pristine substrate, with the coverage and substrate temperature chosen such that the island size and areal density are as desired. The growth is then continued with the shell material, with the temperature chosen such that impinging atoms attach to and completely decorate the existing islands. Ideally for the growth of core–shell particles, diffusion along step edges and around corners, as well as step descent, is enabled. An example is monolayer-high Co–Pt core–shell islands, where compact Pt islands have been formed by Pt deposition at 130 K and post-annealing to 760 K, followed by decoration with a three-atom-wide Co shell by Co deposition at 220 K [54].

2.1.3. Post-annealing and alloy formation. The nucleation regime is ideal for the synthesis of very small clusters comprising just a few atoms. The size distribution is then characterized by a standard deviation roughly scaling as $\langle n\rangle^{1/2}$, where n is the number of atoms per island. These size distributions are often sufficiently narrow to explore the size dependence of the physical and chemical properties of metallic nanostructures, such as their magnetism [29]. Larger particle sizes with substantially narrowed size distribution, $0.3\langle n\rangle$, can be synthesized by the Ostwald ripening technique [55]. Here, already nucleated islands of a given size distribution are annealed in order to initiate ripening, i.e. a growth of the larger islands by drawing material from the smaller ones [56].

The post-annealing of aggregates at sufficiently high temperatures can also promote intermixing of aggregate and substrate and result in surface-confined ordered alloys. Adlayers of Co or Fe, for instance, form an alloy with a Pt substrate, which is restricted to the topmost surface layer at intermediate annealing temperatures of 500–550 K [57–59] (see also figure 4 and section 2.2.1). Such surface alloys are therefore metastable. Formation of surface alloys have also been reported for a variety of other materials, including CuPb on Cu(111), CuAu surface alloys on Cu(100) and PtCo alloys on Pt(111) [59]. In section 4.3 we will see that the local atomic arrangement in FePt surface alloys depends critically on the Fe concentration and determines its magnetic properties [60].

2.1.4. Cluster deposition. The self-assembly and structure formation during molecular beam epitaxy (MBE) strongly depends on the substrate itself, as discussed above. Mainly two techniques have been developed to turn off the substrate's influence during growth: the soft-landing of gas-phase clusters [13] and the buffer-layer-assisted cluster growth (BLAG) directly at the surface [61–63]. Both techniques are, in principle, suitable to form clusters of almost any material on any substrate [64, 65], without the implications associated with epitaxy. The clusters are formed before they make contact with the substrate and their initial structure is not impeded by the surface [66]. However, the final shape and structure as well as the size and spatial distribution of the clusters after landing can be strongly affected by surface wetting and diffusivity [67] (section 4.4.1). The main advantage of BLAG over other cluster deposition methods is that no experimental equipment beyond the standard MBE tools is required. Furthermore, the formation of the cluster layer is a parallel process and high cluster coverage can be achieved in a short time. In contrast, the cluster flux of dedicated cluster sources is limited by the mass filtering. This increases the deposition time considerably, but usually yields narrower cluster size distributions. Recent overviews of fabrication and properties of surface-supported clusters can be found, for instance, in [68, 69].

Buffer-layer-assisted cluster fabrication, pioneered by Weaver *et al* [61], requires pre-coating the substrate by a noble gas layer, such as Xe, at low temperature. Metal atoms are mobile on this buffer layer and form small clusters [63]. Warming up the substrate to 55 K causes the evaporation of the bulk Xe layer. The last layer of Xe in direct contact with the substrate is thermally more stable and substrate temperatures of approximately 100 K are necessary for complete desorption [67]. The clusters coalesce during the Xe sublimation and thus grow in size, until they make contact with the surface. The final cluster size and size distribution depend mainly on the initial thickness of the Xe layer and on the metal coverage. The deposited particles can be randomly oriented, but if the cluster wets the surface then the surface structure will dictate the cluster structure. The advantage of this deposition method is in its potential to fabricate ordered arrays of clusters on template surfaces, as discussed in section 2.2 [70, 71, 9].

2.1.5. Supramolecular structures. Flat metal surfaces are ideal for the fabrication of 2D molecular nanostructures

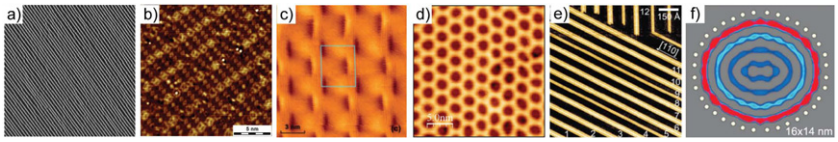

Figure 3. Template surfaces for guided nanostructure self-assembly. (a) Regularly stepped Pt(997) [74], (b) 15 × 12 surface reconstruction of C/W(110) [75], (c) misfit dislocations in one Ag(111) monolayer on Ru(0001) [76], (d) corrugated boron nitride monolayer [77, 70], (e) methionine biomolecular nanogratings on Ag(111) [78] and (f) quantum confinement of surface state electrons [79].

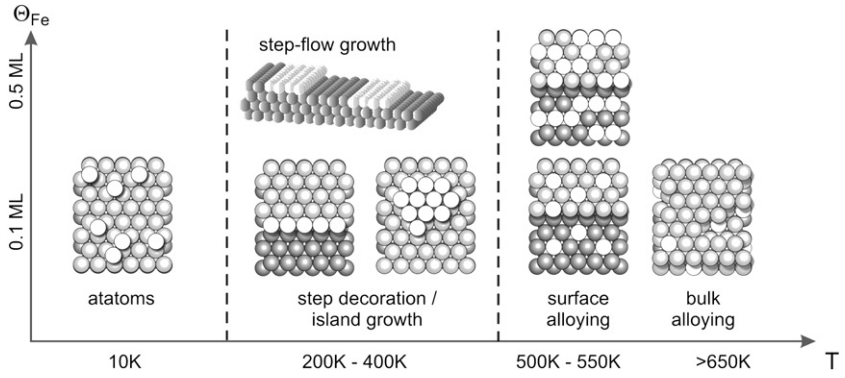

Figure 4. Top view on magnetic Fe–Pt surface structures (schematic). The brightest colors represent Fe atoms, while darker colors represent Pt atoms in different layers. A variety of different Fe–Pt nanostructures can be fabricated by controlling only the substrate temperature during Fe deposition (T) and Fe coverage (θ_{Fe}). The increased mobility at higher temperatures promotes chain or stripe formation on Pt(997) or compact cluster formation on Pt(111), and eventually surface and bulk alloying [57].

by self-assembly, following the principles of supramolecular chemistry. Supramolecular chemistry is widely used to synthesize molecular crystals or other supramolecular compounds in solution. In analogy to the well-known 3D supramolecular chemistry, non-covalent interactions, such as van der Waals interactions and hydrogen bonding, also govern the molecular self-assembly of 2D networks on crystalline surfaces. The molecules can be brought into contact with the substrate surface by thermal evaporation, from solution [72], by contact printing [15] or by electrospray ionization deposition [16]. Control parameters for the self-assembled growth are the design of the molecules and their functional groups, the stoichiometric ratio of molecules and other metal atoms or linker clusters, as well as the temperature. However, the substrate will set limits to the mobility of the adsorbed molecules, may alter their electronic structure or the substrate's electronic states at the surfaces may become perturbed locally. A consequence is that the established concepts of solution-based coordination chemistry cannot be applied without appropriate modification [73]. The substrate thus becomes an important additional parameter to steer the molecular self-assembly and to control the final architecture of the networks.

2.2. Nanostructures on template surfaces

Patterned, structured and textured surfaces can be used as templates to control the nucleation of adatoms or to provide additional barriers to the diffusion of atoms, and hence to control the shape and size of the growing aggregates. Commonly, a distinction is made between *natural* and *artificial* template surfaces. Natural nanotemplates are surfaces that have spontaneously developed a particular morphology, to minimize the surface or elastic energy, such as stepped or reconstructed surfaces, strain relief patterns and surface corrugations. Flat surfaces that favorably mediate electronic effects can also be used to direct the nanostructure growth. In contrast, artificial template surfaces are created by top-down or bottom-up strategies. An example of simple artificial structuring is the grooving of the substrate surface by directional mechanical polishing [80]. However, nanostructures themselves can also serve as templates for further growth of more complex or 3D structures. One example is surface-supported biomolecular gratings [78].

More generally, all top-down fabrication techniques can be applied to the fabrication of prestructured substrates [81], especially if spacings larger than a few nanometers are needed. The advantage of artificial templates is that they can be tailored with greater flexibility to exhibit desired patterns of nucleation sites or diffusion channels. However, only natural templates are useful to fabricate the smallest and monodisperse nanostructures with atomic precision and separations of only a few lattice spacings. Surface patterns like those summarized in figure 3 provide predefined energetic sinks for the preferential nucleation of deposited atoms [82, 81, 83]. The position of each nanostructure is thus exactly defined by the template, with spacings ranging from a few ångströms up to a few nanometers. A valuable side effect of the nucleation and growth on such patterned substrates is the typically enhanced size uniformity, in comparison to nanostructures on flat substrates. In the following, we will discuss examples of nanostructure growth on natural templates.

2.2.1. Terrace steps and kinks. Stepped and kinked surfaces are commonly employed as templates for the synthesis of quasi-one-dimensional systems [84, 85], such as atomically thin metal stripes and chains of atoms [43, 86, 87, 74, 88, 89], structured sesquilayers [90], cluster chains [9, 91] and dot arrays [92, 80]. The template effect is based on the higher binding energy at the steps, in comparison to terrace sites. The mobility of a deposited atom on its random walk is reduced by encounters with a step edge due to higher coordination there or due to a Schwoebel–Ehrlich barrier [93]. Depending on the system, atoms can attach at the bottom or at the top of the step edge. If the atoms have sufficiently high diffusivity along the step edges then row-by-row step flow growth is observed during MBE growth [84]. By controlling the adlayer coverage, stripes of controllable width down to monatomic chains can be easily prepared [74]. Growth of ideal 2D systems can be achieved by the presence of substrate steps if the growth proceeds in the step flow growth mode. At higher substrate temperatures, the step edges represent penetrable defects for adatoms to enter the surface layer of the substrate. This has been exploited, for instance, to form 2D FePt surface alloys [57, 8].

As an example of nanostructure growth on stepped substrates, we discuss here Fe structures on Pt substrates. Fe and Pt are known to form structurally and magnetically interesting bulk alloys, such as Fe_3Pt (cubic Cu_3Au structure) and FePt (tetragonal $L1_0$ structure). However, growth of Fe on Pt substrate surfaces offer new possibilities to stabilize other Fe–Pt structures that do not occur naturally in bulk materials. The step edges play a key role in this process. Several well-defined Fe structures can be synthesized from sub-monolayer coverages of Fe on Pt(997), by exploiting the substrate steps, while on flat Pt(111) rather ramified Fe islands are formed [66, 94]. Hence, by controlling the substrate orientation, the growth temperature and the Fe coverage, a variety of low-coordinated structures, such as atoms, small clusters, chains and stripes of Fe on Pt, as well as ordered or disordered FePt surface alloys can be formed [57, 94, 8]. Figure 4 illustrates some typical examples. Since the local atomic environments in these structures are all different from each other, they represent ideal model systems to study coordination and size effects on magnetism during the crossover from zero to two dimensions [8]. The interaction between Fe and the Pt substrate has a decisive influence on the magnetism and can be exploited to tune the magnetic properties of low-dimensional structures, discussed in section 4.

2.2.2. Surface reconstructions and strain relief patterns. Strain relief patterns are changes in the atomistic structure at the surface of a crystalline substrate or in a thin film, to reduce the elastic energy due to a lattice mismatch, surface tension or alloying. Typical strain relief patterns are misfit dislocation networks [95, 75], incommensurate structures [96] and surface 'buckling' [97, 77]. Also some types of surface reconstructions are formed primarily to reduce the elastic energy [98]. Misfit dislocation networks or reconstructions of crystalline surfaces provide excellent opportunities to grow ordered arrays of nanoclusters by direct deposition, since the impinging adatoms preferentially nucleate at distinctive sites of the surface structure. Numerous examples demonstrate that ordered arrays of nanodots or otherwise ordered structures can be formed on misfit dislocations, such as Fe islands on atomically thin Cu films on Pt(111) [82], Fe and Co on carburized W(110) [99], Fe on Cu(111) [100] or on Cu_3N–Cu(110) molecular networks [101], Co on strained Pt(111) films [76] and many others. Furthermore, surface reconstructions, such as the famous 'herringbone'-type reconstruction of Au(111) and reconstructions of the Pd(110) or Ir(100) surfaces, have provided the basis for directed growth to create ordered nanostructure adlayers in a variety of experiments. Examples are the synthesis of atomic wires of Fe on Ir(100) [98] or Cu on Pd(110) [55], or 2D Co dot arrays on Au [102].

Growth guided by strain relief patterns has further been achieved using insulating adlayers, such as Cu_3N monolayers on Cu(110), thereby decoupling the nanostructures electronically from the substrate [101]. Particularly intriguing is the use of corrugated boron nitride (BN) layers to fabricate ordered arrays of Co clusters [70, 71]. Such BN layers grown on Rh(111) exhibit a strain-driven hexagonally ordered corrugation with a periodicity of 3.2 nm [77, 103, 70], as can be seen in the scanning tunneling microscopy images in figure 3(d). The BN layers are atomically thin, electrically insulating, chemically inert and mechanically extremely stable, and are thus ideal as templates for nanostructure growth. Recent STM and theoretical work has shown that the BN layer is buckled due to epitaxial strain and only locally attached to the Rh surfaces [103, 104]. Such BN layers are commonly referred to as nanomeshes, but they rather resemble an array of muffin tins. The difference in height between the attached areas (depressions) and the detached ridges is approximately 0.55 Å for BN on Rh(111) [104]. BN layers have been used as templates for the controlled positioning of nonmagnetic molecules, such as C_{60} or naphthalocyanine, 'nano-ice' [105] and more recently for the synthesis of ordered arrays of Co clusters by buffer-layer-assisted growth [70, 71]. The latter approach combines the versatility of the cluster deposition from the gas phase with the positional accuracy of directed, self-assembled growth. It thus represents a promising and viable strategy for the fabrication of ordered nanodot layers of virtually any material [64, 65].

2.2.3. Moiré patterns. A moiré pattern is formed when a monolayer thin film grows commensurately on a substrate, with both lattice constants being just slightly different. The periodicity of the moiré pattern is typically several lattice spacings, and dependent on the lattice mismatch and the angle between film and substrate. Systems that form a moiré pattern are, for example, hexagonal BN layers on Pt(111) [106], Pd(111) [107] or Pd(110) [108], FeO(111) double layers on Pt(111) [109], NaCl bilayers on Cu(111) [110, 111], Sm(0001) on W(110) or Eu monolayers on Gd(0001) [112], graphene on Ir(111) [113, 114] and two mismatched graphene sheets [115]. Moiré patterns result in periodic oscillations of the surface potential, or the electronic local density of states [116] and this can provide preferential adsorption sites for metallic

adsorbates, thereby templating the adlayer growth. The self-assembly of Au atoms on an FeO/Pt(111) moiré pattern, for instance, is the consequence of an inhomogeneous surface potential within the FeO moiré cell and substantial electrostatic repulsion between the adatoms [110]. The corresponding electrostatic repulsion is discussed in section 2.3. Other examples for structural self-organization guided by moiré patterns is the ordering of Ir clusters on a graphene moiré on Ir(111) [117] or the adsorption of Ag atoms on NaCl bilayers on Cu(001) [111].

2.3. Self-ordering due to long-range interactions

Other strategies to achieve ordered arrangements of small structures are based on the control of attractive and repulsive interactions between atoms, molecules or clusters to promote ordering and structure formation *on flat surfaces*. At small separations, direct electronic interactions dominate and may directly lead to the formation of chemical bonds, but at larger separation, interactions are mediated either by electrostatic (dipole–dipole) and elastic (deformation of substrate lattice) fields [118, 119] or by surface electrons. Such interactions can be exploited for nanostructuring or self-ordering without chemical bond formation, as will be discussed next.

2.3.1. Electrostatic and charge transfer effects. Electrostatic self-assembly refers to the synthesis of layered or otherwise ordered structures of mostly organic materials by exploiting attractive or repulsive electrostatic forces [120]. This method has been used, for instance, to fabricate layers of Fe_3O_4 nanoparticles [121], but more commonly for the fabrication of self-assembled monolayers of complexes of polymers, oxide nanoclusters, cage-structured molecules such as fullerenes, and proteins and other biomolecules. However, the ordering of surface-supported metallic nanostructures can be influenced by electrostatic forces if the ad-structures are either isolated from the metallic substrate by an insulating interlayer or noble gas buffer layers, or if the forces are a result of charge screening by the substrate. Examples of the latter are the formation of ordered arrays of Ag clusters on carburated W(110) [122], the self-organization of Au atoms on FeO(111) surfaces [110], the interaction between Cu atoms and dimers on Ag(111) [119], and the 2D condensation of K atoms on Cu(100) or Al(111) [123, 124].

Electrostatic forces can determine the self-assembly of molecular surface-supported systems, such as those described in section 2.1.5. This is typically the result of charge transfer between the organics and the metal substrate, by which a surface dipole is formed. This can either promote ordering, as in the case of 2D self-assembly of 1-nitronaphthalene on Au(111) [125] or tetrathiafulvalene on Au(111) [126], or prevent self-assembly, as observed for TCNE molecules on Ag(110) [127] or TPP on Cu(111) [128]. The latter occurs if the spacing between two adsorbates is too large for attractive interactions to become effective. For molecular adsorbates, this is the case for spacings larger than 16 Å [129].

2.3.2. Substrate-mediated self-assembly. Substrate-mediated interactions between surface-supported atoms involve the electrons in the substrate surface, most importantly the surface state electrons on the (111) surface of noble metals that form a two-dimensional nearly-free electron gas. The surface state electrons limit the motion of the adatoms by modifying the diffusion potential, thereby influencing the growth [119]. Typically, the scattering of such electrons leads to quantum interference patterns in the local density of states and to long-range Friedel-type oscillatory interactions between the adsorbates. This results in attractive or repulsive interactions, depending on the spacing [130]. These interactions are well known to be of significant magnitude over distances as large as several tens of interatomic spacings. An interesting feature is that substrate-mediated interactions can promote magnetic ordering of the adatoms, as has been described in theory by Ignatiev *et al* in [131] and studied recently in experiments by Zhou *et al* of Co adatoms on Pt(111) [132].

Reported energies for substrate-mediated interactions are of the order of one or more millielectronvolts (meV) over a distance of a few nanometers. Examples include Cu adatoms on Cu(111) and Ce on Ag(111) (1 meV at 1–2 nm) [133–136], Re on W(110) (15 meV at 1–2 nm) [137] and Br islands on Cu(111) (25 meV at 2 nm) [138]. Since those energies are lower than the thermal energy at room temperature ($k_BT \approx$ 25 meV), self-assembly mediated by surface state electrons is usually observed at low temperatures [136, 139]. The magnitude of the energy barriers for single-atom diffusion on surfaces is, in contrast, of the same order or higher, and can be as high as 9 meV for Ce adatoms on Ag(111) [136, 140] and 37 meV for Co adatoms on Cu(111) [141]. Thus, the subtle balance between sample temperature, adatom diffusion barrier and interaction potential is of critical importance for controlled structure formation [140].

Around single adatoms, the electron density oscillates due to scattering, so that the interactions between two adatoms are also oscillatory and vary with distance. They are attractive if the distance between the two adatoms matches the periodicity of the Friedel oscillations [142]. This mechanism is used for 2D superlattice formation from adatoms at surfaces, such as Ce atoms on Ag(111) and 3d element atoms on Cu(111) [143].

Substrate-mediated self-assembly can be further controlled by surface state electron confinement with closed or open quantum resonator structures, to affect the atomic diffusion and control structure formation [139]. A variety of artificial structures has been fabricated this way, including 1D chains of atoms [144, 139, 89, 78], triangular systems [145] or more complex patterns such as 'quantum onions' [146].

2.4. Other deposition and sculpting methods

As a closing paragraph of this section on synthesis let us briefly discuss some alternative approaches to fabricate surface structures for the *in situ* study of nanomagnetism. As of today, these alternative methods are niche strategies, less widely used than those in the previous sections, but this does not mean that the structural quality achieved by these methods is lagging behind. However, these methods are often less suitable for

metals or work only for particular materials or classes of materials, do not offer sufficient structural control or are too time-consuming.

Single-atom manipulation and STM lithography. Scanning tunneling microscopes have been used to build artificial structures from single atoms or molecules, ranging from tiny clusters [6] and chains of atoms [147] to quantum corrals [148] and more complex structures [149, 150]. This approach permits us to build lateral structures of virtually any atomic configuration with the greatest accuracy by exploiting and controlling the forces between the tip of the STM and adsorbates [151, 152]. The structure fabrication is a sequential process and thus slow, as only one atom or molecule is moved at a time. Also, atomic surface diffusion needs to be suppressed by keeping the substrate at low temperatures, typically liquid helium temperatures. This method works best for weakly bound adsorbates, such as noble gas atoms or small molecules, and is not suitable if the adsorbate's binding energy to the substrate or the migration barriers are high. Examples of other applications of STM for local structuring include laterally enhanced lithography [153], local electrodeposition [154] or nanoscale metal cluster deposition [155]. These approaches cannot usually compete with self-assembly strategies in regards to speed and structural control, but have the advantage of locally controlled fabrication for subsequent local probe studies.

Shadow mask lithography is used to fabricate uniform simple metallic structures, such as dots, rods or rings, over very large sample areas [156, 157]. This method is based on MBE deposition of metals on a surface that is pre-covered by nanospheres, such as polystyrene spheres, followed by the removal of the spheres. Dots are formed on the uncovered areas of the substrate and structural control can be achieved through changing the mask morphology by temperature processing and varying the evaporation conditions. This approach is very efficient for the fabrication of structures of 200–30 nm in size, and this limit is mainly set by the availability of nanospheres for the mask.

Dry imprinting. This method permits the deposition of material under UHV that may not be thermally evaporated, such as single molecular magnets [15]. A soft applicator, such as a fiberglass bundle, is coated with fine-grained powder of the substance of interest and brought into gentle contact with the substrate using a push–pull feedthrough. The molecules are initially disordered but ordering can be promoted by thermal treatment.

Sputter-induced patterning. Symmetric hexagonal or square patterns of dots, holes or ripples can be fabricated from almost all materials, including insulators, metals or even organic materials by ion-beam sputtering. Here, surfaces or thin films are sputtered with one or more low-energy ion beams, applied to the sample under varied angles simultaneously or sequentially [158, 159].

3. Fundamental aspects of nanoscale magnetism

Neither macroscopic nor atomic physics are able to explain the magnetism of nanostructures interacting with metallic substrates, because many nanoscale effects go beyond a superposition of quantum-mechanical and macroscopic phenomena. This section provides a theoretical introduction to some key phenomena and mechanisms governing the behavior of nanostructures considered in this review. Among the discussed examples are the electronic structure of confined structures, emerging magnetism, critical fluctuations in small-scale structures, mesoscopic Kondo effects and non-collinear structures.

3.1. Electronic structure

In a nutshell, the electronic structure of nanostructured magnets is given by the interatomic hopping of d and other electrons subject to geometric and chemical constraints. The hopping corresponds to a hybridization of the electron wavefunctions and yields, very often, an energy gain. The easiest way to rationalize this hybridization energy is to take into account that the kinetic energy of an electron confined to a box of size b scales as $1/b^2$. Hopping to neighboring atoms effectively increases the size of the box and reduces the kinetic energy. Nanostructuring limits the extent of this electron delocalization and leads, for example, to electron confinement in nanoparticles and to various magic number effects associated with discrete energy levels.

3.1.1. Basic features. A simple but instructive electronic-structure model is two atoms of the same kind, labeled left (subscript L) and right (subscript R), and wavefunctions $\phi_{\mathrm{L}}(\mathbf{r}) = \phi(\mathbf{r} - \mathbf{R}_{\mathrm{L}})$ and $\phi_{\mathrm{R}}(\mathbf{r}) = \phi(\mathbf{r} - \mathbf{R}_{\mathrm{R}})$. As the atoms come closer together, the two wavefunctions hybridize and the corresponding tight-binding Hamiltonian is

$$H = \begin{pmatrix} E_0 & t \\ t & E_0 \end{pmatrix}. \tag{2}$$

Here E_0 is the orbital energy of the non-interacting atoms and the matrix element t is the hopping integral. The diagonalization of equation (2) is well known from the H_2^+ problem and yields two hybridized wavefunctions $\psi(\mathbf{r}) \sim \phi_{\mathrm{L}}(\mathbf{r}) \pm \phi_{\mathrm{R}}(\mathbf{r})$ and a level splitting into bonding and antibonding states of energy $E_0 \pm t$. More generally, a system with N atoms and n orbitals per atom has $n \times N$ hybridized wavefunctions, each of the type $\psi(\mathbf{r}) = \sum_{\mu i} c_{\mu i}\phi_{\mu}(\mathbf{r} - \mathbf{R}_i)$. As for equation (2), the expansion coefficients $c_{\mu i}$ are obtained by matrix diagonalization. The corresponding density of states, which determines the onset of ferromagnetism, can be a collection of discrete sharp peaks (as in free clusters), a continuum (for example in nanowires) or a combination of both.

In perfect solids, one can exploit the periodicity of the lattice and the Bloch symmetry of the wavefunctions, which leads to energy bands $E_{\mu}(\mathbf{k})$ whose width is of the order of t. Nanostructures contain surfaces and interfaces, so that the periodicity is broken and the electronic structure goes beyond continuous bands. For example, in nanoparticles, the continuous bands must be replaced by narrowly spaced energy levels. On a tight-binding level [160], the treatment of nanostructures is straightforward, and equation (2) is easily

extended to several thousand atoms. For accurate calculations it is better to use advanced methods such as the local spin density approximation (LSDA) [161–163].

3.1.2. Correlation effects. Pairs of electrons located at $\mathbf{r}_i$ and $\mathbf{r}_j$ experience the Coulomb interaction:

$$V_{12}(\mathbf{r}_i, \mathbf{r}_j) = \frac{e^2}{4\pi\epsilon_0|\mathbf{r}_i - \mathbf{r}_j|}. \quad (3)$$

As mentioned in the introduction, this interaction is of great importance in magnetism, because it is essentially responsible for the formation of atomic moments. There is no explicit spin dependence in equation (3), but the Pauli principle affects the $\uparrow\uparrow$ and $\uparrow\downarrow$ wavefunctions in a different way, yielding different energies for FM and AFM configurations. For methods to cast the seemingly spin-independent Coulomb energy into the form of a spin Hamiltonian (Heisenberg Hamiltonian), see, for example [164]. Since the number of electrons in a solid or nanostructure is large, equation (3) establishes a complicated many-body problem and approximate methods must be used to treat the Coulomb interaction in magnetic solids and nanostructures. Density-functional theory (DFT) determines the ground-state energy for arbitrary crystal potentials and, if the density potential was known exactly, the ground-state energy would be correct. However, neither excitation energies nor the ground-state wavefunction can be determined by DFT and this method, as well as simpler methods such as tight-binding and LSDA, treat the Coulomb interaction between electrons on a quantum-mechanical mean-field level. In this independent-electron approximation, an electron at $\mathbf{r}$ interacts with an average potential $V_{\text{eff}}(\mathbf{r})$ created by all other electrons, rather than with individual electrons $\mathbf{r}_i$. This is a highly simplified description of electron correlations and means, for example, that DFT 'wavefunctions' are tools to determine the electron and spin density rather than wavefunctions in a quantum-mechanical sense. Similar arguments apply to the Stoner model, where $I \sim V_{12} \sim V_{\text{eff}}(\mathbf{r})$ is a mean-field interaction parameter.

An example of a true many-body or correlation effect is spin–charge separation [165, 166], which means that charge and spin degrees of freedom are well separated and characterized by high and low excitation energies, respectively. Neither charge nor spin excitations are within the scope of density-function theory, but methods aimed at better treatment of correlations, such as LSDA + U, SIC (self-interaction correction) and DMFT (dynamic mean-field theory) may give quite accurate ground-state configurations (atomic charges) without necessarily reproducing the spin structure (multiplets). The character of correlation effects is seen from the J mixing of Sm 4f electrons in metallic magnetic materials, such as $SmCo_5$, which is important for the understanding of anisotropy, but goes far beyond the independent-electron approach [30]. In a strict sense, the anisotropy is a ground-state effect, because the energy is minimized for different magnetization directions and then analyzed as a function of the magnetization angle. However, the $J = 5/2$ ground state of the Sm^{3+} ion and the lowest-lying excited multiplet ($J = 7/2$) yield drastically different sixth-order anisotropy contributions. DFT is not equipped to handle such quantitative higher-order anisotropy changes, or even to predict the huge lowest-order anisotropy of $SmCo_5$.

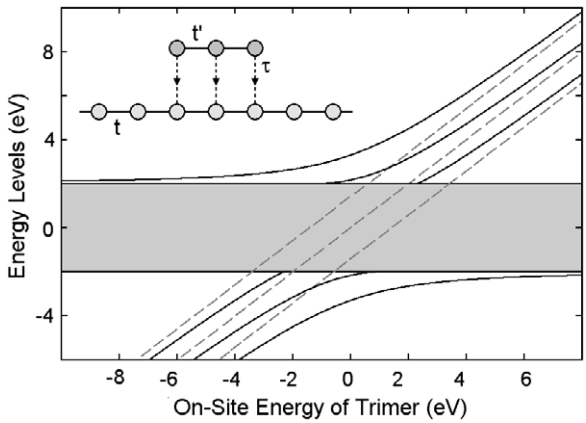

Figure 5. Proximity effect for a trimer interacting with an atomic chain. The dashed lines are the levels of the non-interacting trimer and the gray area is the energy band of the chain.

Compared to rare-earth magnets and oxides, correlation effects in metallic 3d-based structures are often less pronounced. In terms of the average distance between electrons, $r_e \sim 1/k_F$, the kinetic energy is proportional to $1/r_e^2$, whereas the Coulomb (correlation) energy scales as $1/r_e$. In metallic high-density electron gases, r_e is small, the kinetic energy dominates and the Coulomb energy is fairly well described by the independent-electron approach. This is the basis for the description of magnetism in itinerant magnets. Note also that nanoscale features of size L become less important, because r_e/L is small. An exception to this rule is the Kondo effect, which involves many conduction electrons and macroscopic length scales (section 3.7).

3.1.3. Nanostructures in contact with extended solids. Interesting scenarios develop when small-scale features such as nanodots come into contact with extended structures, such as thin films and surfaces. In general, the conduction (or valence) electrons of surface and dot atoms have very different orbital energies E_s and E_d, respectively. The surface levels (E_s) typical broaden into bands of width W. If E_d is much larger than $E_s + W/2$, or much smaller than $E_s - W/2$, then there is little interaction between the adatom and surface. This non-bonding case is not very interesting, but a rich physics develops if $E_d \sim E_s$.

Figure 5 shows the electronic structure of a trimer of s atoms coupled to a chain of atoms. The distance between trimer and chain is kept constant, corresponding to a fixed hopping integral τ between chain and trimer atoms, but the orbital energy (on-site energy) of the trimer changes. In the absence of the atomic chain, the s states of the trimer split into triplets (dashed lines). The interaction with the chain causes the trimer and chain states to hybridize. Figure 5 shows that the low-lying trimer states (solid lines) reduce their energy compared to the non-interacting trimers, which corresponds

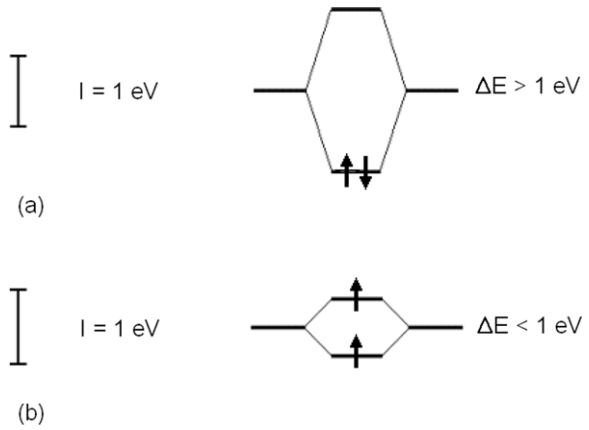

Figure 6. Magnetism and one-electron level splitting: (a) paramagnetic and (b) ferromagnetic spin alignment. The effective Coulomb interaction is of the order of 1 eV (the Stoner parameter I in metals), whereas the level splitting strongly depends on the atomic environment.

to chemical bonding. An interesting feature of the trimer levels is their localization. The localization length of the trimer states increases as the levels approach the band and becomes infinite when the lines cross the band edge. This delocalization corresponds to a broadening of the sharp dot levels into resonances [167, 168].

3.2. Magnetic moment and magnetization

Let us now return to the formation of atomic moments due to the Coulomb interaction, with the aim of discussing the influences of chemistry and the atomic environment. In any given orbital, the Pauli principle allows electrostatically unfavorable $\uparrow\downarrow$ pairs but forbids $\uparrow\uparrow$ pairs. If the Pauli principle and the Coulomb interaction were the only considerations, then all materials would be ferromagnetic, but the creation of an $\uparrow\uparrow$ pair means that one electron must occupy an orbital with enhanced one-electron energy. Most materials are actually nonmagnetic, because the electrons fill the available low-lying one-electron states with $\uparrow\downarrow$ pairs. An exception is electrons in the partially filled shells of transition-metal atoms, which are nearly degenerate and susceptible to moment formation.

In metals, the effective strength of the Coulomb interaction is given by the Stoner parameter $I \approx 1$ eV, so that the formation of a ferromagnetic moment is favorable for narrow bands with hybridization energies smaller than about 1 eV. Figure 6 illustrates this point by showing the one-electron level splittings for a two-electron system. Typical 3d metals have a bandwidth $W \approx 5$ eV, but their densities of states (DOS) exhibit sharps peaks that have widths ΔE of less than 1 eV. A refined version of this argument is the Stoner criterion $I D(E_F) > 1$, where $D(E_F)$ is the DOS at the Fermi level. The DOS scales as $1/W$ and is roughly proportional to the inverse square root of the number z of nearest neighbors [162, 30]. Physically, a reduced z leads to reduced hybridization and facilitates moment formation at surfaces and in small-scale nanostructures.

The Stoner theory is an independent-electron approach and means that electrons in narrow bands exhibit a spin orientation to be parallel to the average spin. The mechanism is also referred to as Stoner exchange, although the Stoner integral (I) is a Coulomb integral involving $\rho(\mathbf{r}) = \psi^*(\mathbf{r})\psi(\mathbf{r}')$ rather than an exchange integral involving $\psi^*(\mathbf{r})\psi(\mathbf{r}')$. It is also important to distinguish intra-atomic exchange, which determines the atomic moment, from interatomic or Heisenberg exchange, which is responsible for magnetic order. Intra-atomic exchange is of the order of 1 eV and usually stronger than interatomic exchange ($\leqslant$0.1 eV), so that the atomic magnetic moment survives above T_C [165, 30]. The Stoner theory is of the intra-atomic type and poorly distinguishes between intra- and interatomic interactions. If used to predict the Curie temperature, it overestimates T_c by several 100%.

The Stoner criterion does not distinguish between paramagnetism and antiferromagnetism (AFM). In practice, empty and nearly filled d bands tend to yield a ferromagnetic spin structure if they satisfy the Stoner criterion. The bandwidth tends to decreases with increasing number of d electrons, so that ferromagnetism is realized in Fe, Co and Ni, as well as in many of their alloys. Elements in the middle of the 3d series, especially Cr and Mn, exhibit a trend towards antiferromagnetism. This is a band-filling effect, caused by different gains in hybridization energies. The hybridization reduces the energies of both FM and AFM spin structures, but the AFM hybridization is less pronounced, because the hopping of $\uparrow$ electrons onto $\downarrow$ sites (or vice versa) costs Coulomb energy. However, ferromagnetic spin polarization of a half-filled shell means that the $\uparrow$ orbitals are all occupied (50% bonding and 50% antibonding orbitals) and that the net hybridization is zero. Antiferromagnets do not suffer from this restriction and their residual hybridization becomes the leading consideration. Non-collinear spin structures are caused by competing FM and AFM interactions. The effect is well known from the rare-earth elements [168, 169] but it also occurs in itinerant ferromagnets [170].

Interesting magnetic effects occur if different atomic species are brought into contact at an interface or in an alloy. Figure 7 illustrates this effect for Co–Pt. Elemental Co is a strong ferromagnet with a completely filled $\downarrow$ band (a), whereas Pt is a Pauli paramagnet with equal numbers of $\uparrow$ and $\downarrow$ electrons. In Co–Pt alloys (b), the site-projected local density is skewed and the Pt exhibits spin polarization. The Pt moment is relatively small but practically important, because Pt possesses a strong spin–orbit coupling and yields a strong magnetic anisotropy per uncompensated spin [29]. We will encounter the consequences of this mechanism in section 4.3.

3.3. Magnetic order in reduced dimensions

A nontrivial question is the onset of ferromagnetism in low-dimensional systems. It can be shown exactly that zero-and one-dimensional 'ferromagnets' are paramagnetic, because thermal fluctuations cause the atomic moments to average to zero [171, 31, 172, 173]. However, a nonsingular Curie-like temperature can be defined by considering spin correlations in nanostructures. Such correlations are fairly well described by mean-field theory.

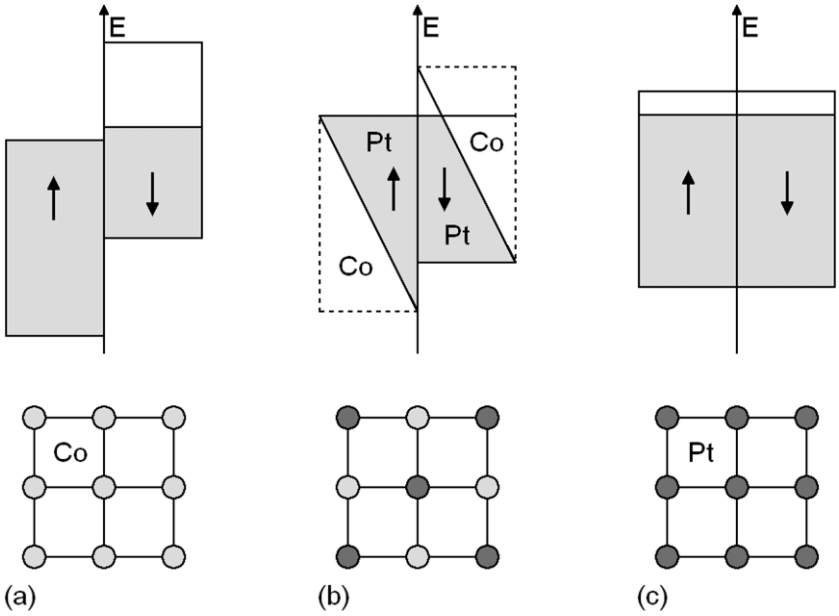

Figure 7. Schematic densities of states for (a) Co, (b) Co–Pt and (c) Pt.

Just below the ordering temperature, the mean-field magnetization m_i of the ith atom obeys

$$k_B T_C m_i = \sum_j J_{ij} m_j \tag{4}$$

where J_{ij} is some effective exchange interaction between neighbors i and j. In homogeneous bulk magnets, $m_i =$ const., so that $\sum_j J_{ij} m_j = zJm_i$ and $T_C = zJ/k_B$. However, the surface breaks the translation symmetry, and missing neighbors as well as changed exchange constants make the spontaneous magnetization inhomogeneous near the Curie temperature. The effect is seen most clearly from the continuum version of equation (4):

$$k_B T m = 2zJm + \frac{J}{2d} a^2 \nabla^2 m. \tag{5}$$

This equation, where a is the interatomic distance, applies to atomic chains ($d = 1$), square, triangular and honeycomb lattices ($d = 2$), and sc, bcc and fcc lattices ($d = 3$). It predicts a Curie temperature smaller than the bulk Curie temperature by a fraction of the order of a^2/D^2, where D is the feature size.

Figure 8 shows the mean-field magnetization distributions in a spherical particle near the Curie temperature. In the model, a common exchange interaction J_{ij} is assumed for both bulk and surface atoms, but the reduced coordination number of the surface atoms effectively reduces the exchange at the surface. At T_c, the magnetization mode $m(\mathbf{r})$ is delocalized (solid line). However, slightly reducing the temperature to $T_c - \delta T$ recovers the intuitive picture of a constant bulk magnetization with a somewhat perturbed magnetization at the surface (dashed line). The value δT depends on the diameter $D = 2R$ of the sphere, scaling as $\delta T \sim 1/D^2$. For a diameter of 10 nm, $\delta T = 20$ K, whereas $D = 0.1$ mm yields $\delta T = 0.2$ μK. This shows that the importance of critical fluctuations rapidly decreases with increasing diameter.

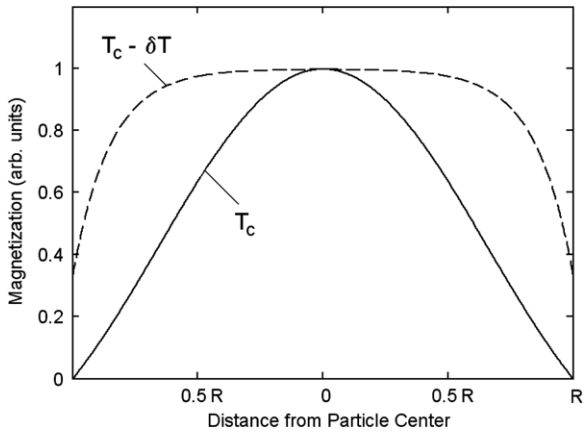

Figure 8. Mean-field magnetization distribution in a bcc-Fe nanoparticle of radius $R = 5$ nm. The dashed line refers to $\delta T = 20$ K.

The above curve applies to materials where the exchange between two neighbors at the surface is the same as in the bulk, so that the reduced coordination at the surface lowers the finite-temperature magnetization near the surface. This is also known as the normal case. Some surfaces, such as Gd(0001), exhibit an enhanced exchange at the surface and a surface transition at $T_s > T_c$ [174, 175]. The opposite, namely a surface transition with $T_s < T_c$, is not possible, even in the bulk. This striking asymmetry arises because the bulk is able to partially polarize a surface below T_c (dashed line in figure 8), whereas the surface is not able to polarize the bulk if $T_c < T < T_s$. It should be noted that the described enhanced T_s, such as that for Gd surfaces, is still under debate; Arnold and Pappas, for instance, reported evidence against it [176], while DFT calculations seem to be in favor of an enhanced coupling [177].

From a broader perspective, figure 8 illustrates how critical fluctuations behave in nanostructures [173] and interact

with geometrical constraints. Mean-field theory predicts a decay or correlation length $\xi \sim 1/|T-T_c|^{\nu}$ with $\nu = 1/2$. This so-called Ornstein–Zernike behavior is easily derived from equation (3), for example by dimensionality analysis. The approximate character of the mean-field approach follows from the critical exponent $\nu > 1/2$, as contrasted with $\nu = 0.71$ for the three-dimensional Heisenberg model, but otherwise the physics is very similar [178]. In this regard, surface nanostructures behave very differently from perfect thin films, where fluctuations destroy long-range order but a small anisotropy is sufficient to stabilize ferromagnetism [179]. In one dimension, that is, in nanowires, even a strong anisotropy is unable to ensure long-range magnetic order [172]. The behavior of two-dimensional surface nanostructures, such as networks, is globally similar to the two-dimensional case but locally more similar to the behavior of nanodots or magnetic molecules. Properties such as $M(H)$ and $M(T)$ curves are largely determined on a local scale, whereas the ferromagnetic low-temperature equilibrium may be difficult to access kinetically. An example of an exactly solvable two-dimensional surface nanostructure is a network of monatomic nanowires [180].

3.4. Magnetic anisotropy

The energy of a magnetic solid depends on the orientation of the magnetization with respect to the crystal axes, which is known as magnetic *anisotropy*. The simplest case is lowest-order (second-order) uniaxial anisotropy energy density $K_1 \sin^2\theta$, where θ is the polar magnetization angle and K_1 is the first-or second-order uniaxial anisotropy constant. K_1 is widely used to describe uniaxial magnets (hexagonal, tetragonal and rhombohedral crystals) and small ellipsoids of revolution (fine particles). For very low symmetry (orthorhombic, monoclinic and triclinic), the first-order anisotropy energy density is

$$\eta = K_1 \sin^2\theta + K_1' \sin^2\theta \cos(2\phi) \qquad (6)$$

where K_1 and K_1' are, in general, of comparable magnitude. The angle ϕ is the azimuthal angle.

While shape anisotropy, caused by magnetostatic interactions, plays a role in some nanostructures [31], the main anisotropy contribution is typically magnetocrystalline anisotropy (MCA). The latter is a relativistic effect, caused by spin–orbit coupling (section 3.6). Our focus is on the itinerant magnetocrystalline anisotropy of 3d, 4d and 5d transition-metal magnets. The determination of the itinerant anisotropy from the atomic structure has remained a challenge, despite the facts that the basic relationship between crystal field or band structure level splitting, spin–orbit coupling and anisotropy has been known for almost a century [181] and that numerical methods have been developed since the 1940s [182, 183].

Magnetocrystalline anisotropy is largely single ion, that is, each d atom yields an individual anisotropy contribution determined by the atom's spin–orbit interaction. Itinerant anisotropy arises from pairs of electron levels that are connected by spin–orbit matrix elements and separated by the Fermi level (or HOMO–LUMO gap). For example, tight-binding states with $|xy\rangle$ and $|x^2 - y^2\rangle$ character yield a pronounced anisotropy contribution along the z axis. The corresponding spin–orbit-induced hybridization is of the type $|\psi\rangle = |xy\rangle \pm i\alpha|x^2 - y^2\rangle$ and carries an orbital moment. In a quasi-classical picture, the spin–orbit coupling creates a circular current (orbital moment) which interacts with the anisotropic crystalline environment (anisotropy). The spin–orbit coupling of the iron-series elements is relatively small ($\lambda \approx 0.05$ eV), so that interatomic hopping easily disrupts the circular current and suppresses the orbital moment. This phenomenon is known as quenching and negatively affects the anisotropy and the orbital moment (section 3.6).

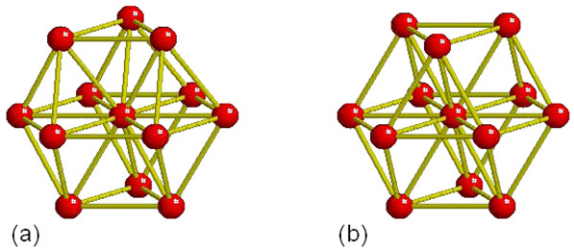

Figure 9. Dense-packed clusters containing $N = 13$ atoms: (a) hcp and (b) fcc. These two structures yield very different anisotropy contributions [184].

The total anisotropy is obtained by summation or integration over all pairs of levels. A striking feature is the existence of many anisotropy peaks and zeros as a function of the number n of 3d electrons per atom (d count). Figure 9 shows two structures with very different anisotropies. The hcp cluster (a) has a pronounced uniaxial anisotropy along the c axis, but the anisotropy rapidly oscillates as a function of n, which can be varied by alloying. The physical reason is that the anisotropy is realized by level pairs enclosing the Fermi energy and the character of these states changes rapidly as the Fermi level is varied. In contrast to the hcp cluster, the uniaxial anisotropy of the fcc cluster (b) is zero by symmetry for all n. An alternative explanation of the huge difference between figures 9(a) and (b) is that small energy differences are important for the determination of the anisotropy, so that distant neighbors are important. In figure 9, the structural difference is the azimuthal orientation of the top and bottom triangles.

3.5. Nanoscale Dzyaloshinskii–Moriya interactions

The spin orientation of many magnetic materials is determined by magnetocrystalline anisotropy, as epitomized by the first uniaxial anisotropy constant K_1. Dzyaloshinskii–Moriya (DM) interactions [185, 186] are of comparable magnitude [187, 188] but require crystals with broken inversion symmetry, such as α-Fe_2O_3, and directly compete with interatomic exchange. A recent finding is spin spirals involving broken symmetries at perfect W(110) surfaces [189]. The cross-product in the Dzyaloshinskii–Moriya interaction:

$$E = \mathbf{D}_{ij} \cdot \mathbf{S}_i \times \mathbf{S}_j \qquad (7)$$

favors a perpendicular spin orientation between neighboring spins and a non-collinear spin structure [190]. In contrast, the Heisenberg exchange $\mathbf{S}_i \cdot \mathbf{S}_j$ favors parallel (or antiparallel) spins. The DM vector $\mathbf{D}$ tends to be much smaller than the interatomic exchange J [168, 31, 187] and experimentally observed non-collinearities tend to reflect competing exchange (section 3.2). Changes of the spin direction due to DM interactions are rather small, typically 1° or less. The same estimate applies to many or most nanostructures with broken inversion symmetry, such as granular composites [31, 187]. However, the situation is different in some nanostructures, such as 2 × 1-ordered Fe–Pt surface alloys, where interatomic exchange, magnetocrystalline anisotropy and DM interactions are all of comparable magnitude, about 0.5 meV [188, 191]. This leads to an intriguing nanoscale interplay between ordinary magnetization states and non-collinear spin structures (see section 4.3).

Consider a DM vector pointing in the y direction parallel to the wires, $\mathbf{D} = D\mathbf{e}_y$, competing with easy-axis anisotropy in the z direction. If the magnetocrystalline anisotropy was the only consideration, then the magnetization would point in the $\pm z$ directions, but the DM favors spin misalignment in the x–z plane, that is, for $(\mathbf{S}_i \times \mathbf{S}_j)_y \neq 0$. Writing the position of the wires at $x_i = ia$ and the magnetization as $\mathbf{M}_i = M_0(\cos\theta_i \mathbf{e}_z + \sin\theta_i \mathbf{e}_x)$ leads, with $\theta_{i+1} = \theta_i + \partial\theta/\partial x$, to

$$\mathbf{D} \cdot (\mathbf{M}_i \times \mathbf{M}_{i+1}) = DM_0^2 a \frac{\partial\theta}{\partial x}. \tag{8}$$

Adding this term to the exchange, anisotropy and external field contributions yields the energy density

$$\eta = A\left(\frac{\partial\theta}{\partial x}\right)^2 + \frac{DM_0^2}{a^2}\frac{\partial\theta}{\partial x} - K_1\cos^2\theta - \mu_0 M_S H\cos\theta \tag{9}$$

and a non-collinear spin structure of periodicity $\lambda = 4\pi Aa^2/DM_0^2$ [188]. Due to the smallness of D, the periodicity is general on the nanoscale. However, the energy behind equation (9) is small, and weak structural or thermal disorder destroys the long-range periodicity. We will return to this interaction in section 4.3.

3.6. Orbital moment

The magnetic moment of the iron-series transition metals is largely given by the spin $\mathbf{s}$ of the 3d electrons, with minor contributions from other electrons and from the orbital moment $\mathbf{l}$ of the 3d electrons. However, the orbital-moment contribution is bigger for heavy transition metals (4d and 5d elements), and experimental methods such as x-ray magnetic circular dichroism (XMCD) also probe 3d orbital moments. As mentioned in the previous paragraph, the nearly complete absence of an orbital moment in many 3d-based magnets is known as quenching and it is instructive to discuss the orbital moment $\mathbf{l}$ and the magnetocrystalline anisotropy (MCA) on an equal footing. Let us consider the Hamiltonian

$$\hat{H} = \hat{H}_0 + \lambda \mathbf{l} \cdot \mathbf{s} \tag{10}$$

where λ is the spin–orbit coupling constant of the d electron. This spin–orbit interaction is obtained from a Pauli-expansion term proportional to $\mathbf{s} \cdot (\nabla V(\mathbf{r}) \times \mathbf{k})$, where V is the one-electron potential and $\mathbf{k}$ is the wavevector of the electrons. The $\mathbf{l} \cdot \mathbf{s}$ form of equation (10) is obtained by assuming a spherical potential $V(\mathbf{r}) = V(r)$, whereas Rashba and Dresselhaus interactions are obtained directly from the $\nabla V(\mathbf{r})$ term. Simplifying somewhat, the unperturbed Hamiltonian $\hat{H}_0$ describes the band structure of the metallic magnet. In non-metallic magnets, which can often be considered as interacting magnetic ions, $\hat{H}_0$ is essentially the crystal field interaction, as in figure 15. The spin $\mathbf{s}$ is essentially equal to the magnetization direction, whereas $\mathbf{l}$ describes the orbital motion of the electrons, which depends on the orientation of the crystal's a, b and c axes. The spin–orbit coupling (SOC) of equation (10) is the origin of both orbital moment and anisotropy. Equation (10) yields the total magnetic energy as a quantum-mechanical average:

$$\langle\Psi|\hat{H}_0|\Psi\rangle + \lambda \cdot \mathbf{s} \cdot \langle\Psi|\mathbf{l}|\Psi\rangle \tag{11}$$

where the wavefunctions $|\Psi\rangle$ do not include the spin part. In lowest-order perturbation theory, $\langle\Psi_0|\mathbf{l}|\Psi_0\rangle = 0$, because $|\Psi_0\rangle$ does not contain orbital currents. Magnetic anisotropy requires higher-order perturbation theory [181], which amounts to the use of wavefunctions $|\Psi\rangle$ with a non-zero orbital moment. Based on this perturbation expansion, and following Bruno [192], it has become popular to equate the spin–orbit energy $E_{SOC} = \lambda\mathbf{s}\langle\Psi|\mathbf{l}|\Psi\rangle$ with the magnetic anisotropy energy (MAE). However, this is a simplistic interpretation of anisotropy and orbital moment. Equation (11) can indeed be written as $E = E_0 + \lambda\mathbf{s}\langle\Psi|\mathbf{l}|\Psi\rangle$, but $E_0 \neq \langle\Psi_0|\hat{H}_0|\Psi_0\rangle$, because the spin–orbit coupling modifies the wavefunction. As a consequence, only a part of E_{SOC} translates into anisotropy and it can be shown that the corrections due to E_0 are substantial. In 3d magnets, the net anisotropy is about 50% of E_{SOC}, whereas in rare-earth magnets, this value decreases to about 1%. A common approach to treat rare-earth anisotropy is actually to extract the anisotropy from $\langle\Psi|\hat{H}_0|\Psi\rangle$, without explicit consideration of the spin–orbit energy [30, 168]. Another counterexample is free transition-metal ions, where a large unquenched orbital moment corresponds to zero anisotropy. Note that the wavefunctions considered in this paragraph are one-electron wavefunctions perturbed by spin–orbit coupling. To find the total anisotropy, one must add the anisotropy contributions of the individual electrons, which is straightforward if one restricts the consideration to second-order anisotropies (force theorem).

The previous paragraph underlines the importance of the crystalline environment, even in 3d magnets. As an example, let us consider $L1_0$-ordered alloys, such as CoPt and FePd. The structure is similar to that of figure 7(b), except that the 3d and 4d/5d atoms form alternating layers. The 3d atoms are largely responsible for the magnetic moment and the Curie temperature and also induce some 4d/5d spin moment, as a precondition for anisotropy. Nearly 50% of the 3d and slightly less than 50% of the 4d/5d spin–orbit energies contribute to the anisotropy, but λ is much higher for the heavy transition-metal atoms, so that most of the anisotropy comes from heavy atoms, even after accounting for the relatively small 4d/5d moment. The atomic environment forms $\hat{H}_0$. The neighbors create

anisotropy by interacting with the 4d/5d orbitals and partially suppress the orbital moment by interfering with motion of the 4d/5d electrons. Note that $\hat{H}_0$ contains contributions from both magnetic and nonmagnetic neighbors, and that surfaces affect the anisotropy in a very similar way.

3.7. Mesoscopic Kondo effect

The Kondo effect, created by magnetic impurities in a nonmagnetic metallic host, has recently attracted renewed attention, fueled by progress in various areas of nanotechnology [193–198]. In bulk materials, the effect is usually associated with the resistance minimum, which was discovered in 1930 by Meissner and Voigt [197] and explained by Kondo in 1964 [198]. The resistivity is characterized by a logarithmic temperature dependence and its explanation involves an integration over all k vectors of the host's conduction electrons [199]. However, the large number of k vectors is only one aspect of the phenomenon, and from a many-body point of view the Kondo effect is caused by competing Coulomb and hopping integrals. It involves a well-localized orbital having a low on-site energy E_0 for the first electron but where the presence of a second electron of opposite spin is punished by a high Coulomb energy [165, 200]. A hopping integral t connects the localized orbital to a single delocalized orbital and yields the system's 'single-orbital' Kondo temperature $T_K = 2t^2/k_B E_0$. Below this temperature, the impurity spin is antiferromagnetic (AFM) coupled to the delocalized electron [165, 200], similar to the AFM interaction of magnetic impurities with the Kondo screening cloud in bulk metals.

3.7.1. Quantum-mechanical origin. Atomically, the Kondo effect arises from the hopping between a localized orbital (magnetic impurity) and one or more delocalized orbitals (conduction electrons) [165, 200]. The energy of the impurity level is lower than that of the conduction electrons by some energy difference E_0. Without electron correlations, the impurity orbital would be occupied by a $\uparrow\downarrow$ electron pair and the impurity atom would be nonmagnetic. However, equation (2) shows that localized and delocalized electrons exhibit very large and very small Coulomb interactions, respectively. The Coulomb interaction in the impurity orbital, $U > E_0$, suppresses the double occupancy, and in fair approximation we can assume $U = \infty$ and single occupancy. In contrast, the small Coulomb interaction of the conduction electrons means that the electron of the impurity atom can temporarily occupy conduction-electron orbitals, so long as this leads to the formation of a $\uparrow\downarrow$ pair. The necessary energy (E_0) is provided by the hopping integral t and the net gain in hybridization energy is $2t^2/E_0$. This energy gain amounts to an AFM coupling between impurity and conduction electrons, because $\uparrow\uparrow$ pairs are forbidden by the Pauli principle and do not contribute to the hybridization. The phenomenon is a low-temperature effect, characterized by the characteristic or 'Kondo' temperature $T_K = 2t^2/E_0 k_B$. More generally, at low temperatures, the magnetic impurity surrounds itself with a screening cloud of conduction electrons of opposite spin. Since the Kondo effect involves spin scattering, the application of a magnetic field weakens the Kondo effect. The same is true for ferromagnetic interatomic exchange in Kondo lattices (heavy fermions) [165], but typical heavy-fermion systems are characterized by low Curie temperatures, so that much of the Kondo physics survives.

3.7.2. Nanoscale implementation. Nanostructuring makes it possible to control the wavelength of the conduction electrons that contribute to the Kondo effect. Consider, for example, a single magnetic impurity is an approximately spherical metal cluster of radius R. The screening cloud, whose size is given by the Kondo coherence or screening length $\xi \sim v_F/T_K$ [198], can be much larger than typical mesoscopic (nanostructural) feature sizes, and the question arises how nanoscale features affect the Kondo effect. In the literature, there are two opposing views. On the one hand, the Kondo effect involves a large number of conduction electrons and this continuum is essential for the understanding of the resistance minimum [199, 184]. On the other hand, the basic quantum-mechanical feature behind the Kondo effect is the interaction of a well-localized impurity spin with delocalized electrons, and this coupling is already realized for a single delocalized or conduction electron [165, 200]. This means that basic features of the Kondo effect survive even for very few electrons. An extreme view is that nanostructuring has little or no effect on the Kondo behavior [201].

In fact, the logarithmic $\ln(T/T_k)$ term in the resistivity reflects the sharpness of the Fermi surface. Perturbation theory [199] means that conduction electrons temporarily occupy states above the Fermi level. The effect is huge at very low temperatures, but the thermal smearing of the Fermi surface means that a typical conduction electron must change its energy by a value of the order of $k_B T$. Nanoparticles do not have a sharp Fermi surface enclosing a continuum of k states but discrete k points in reciprocal space and a gap between the highest occupied (HOMO) and lowest unoccupied (LUMO) states. When $k_B T_K$ becomes smaller than the typical energy spacing Δ between k points, then the Kondo effect cannot fully develop. This happens for particle radii R_K smaller than about $W/k_F k_B T_K$ [184]. Basically, R_K is equal to the size ξ of the Kondo screening cloud. Past efforts to experimentally verify the relation between feature size R and Kondo coherence length ξ have been inconclusive [196, 198]. In our opinion, a fundamental reason for these difficulties is the interference by unconfined conduction electrons in the investigated wire and thin-film structures.

The above effect, caused by magnetic impurities in clusters and constrictions, is only one Kondo mechanism in surface nanostructures. Atoms or dots on surfaces interact with the substrate and yield a type of Kondo effect realized by the conduction electrons of the substrates, in general both bulk and surface state (section 4.1.2). It is possible to directly measure Kondo resonances of nanostructures such as atomic contacts, for example by STM [193, 194, 197], but more direct would be to measure the magnetic susceptibility of magnetic impurities in metallic nanoparticles. It is well known that the bulk Kondo effect leads to a strong reduction of the low-temperature magnetic susceptibility χ [201, 202], as compared

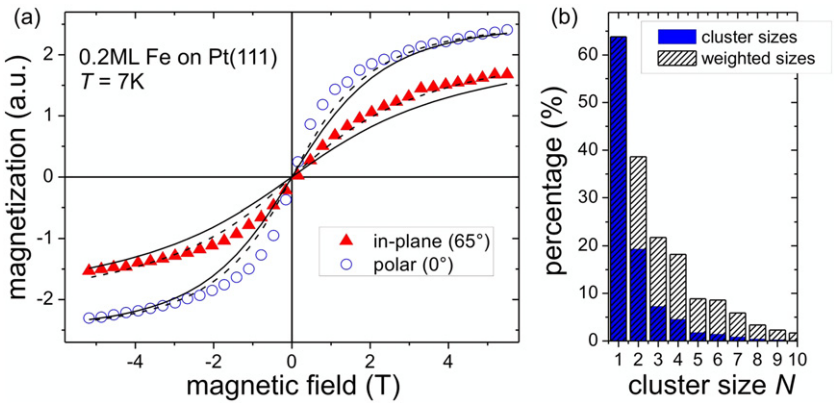

Figure 10. (a) Magnetization curves $M(B)$ (dots) of an ensemble of Fe_N clusters on Pt(111), measured by x-ray magnetic circular dichroism at $T = 6$ K for magnetic field $M(B)$ along the surface normal ($\theta = 0°$) and in-plane direction ($\theta = 65°$). The solid lines are simulated magnetization curves based on the Langevin formula. This simulation is based on calculated cluster-size-dependent anisotropy energies from *ab initio* density-functional calculations [203], as well as on the cluster size distribution in (b). Fe_N clusters with $N \leqslant 3$ (full line) and $N \leqslant 4$ (dashed line) Fe atoms were included in the simulation. (b) Cluster size distribution from a Monte Carlo simulation for nominally deposited 0.2 ML Fe.

to the Curie law $\chi = C/T$, and that the drop starts in the vicinity of the Kondo temperature.

4. Experimental magnetism of simple and complex structures

In this section, we discuss the investigation of magnetic surface nanostructures with scanning tunneling microscopy, x-ray magnetic circular dichroism (XMCD) and the magneto-optical Kerr effect (MOKE). Our focus is on supported nanostructures whose new physics derives from the interaction with the substrate. This includes studies on impurity atoms, one-dimensional chains and stripes, two-dimensional surface alloys and nanometer-size compact clusters. The examples show that interesting physics can especially be expected if the interaction with the substrate is strong, as epitomized by the substrate-dictated anisotropy in Fe and Co impurities, chains and nanometer clusters, increased magnetic anisotropy following alloying and the occurrence of Kondo physics. In contrast, the magnetic behavior is fairly simple in nanoclusters that are decoupled from the substrate. For a third group of structures, which includes 4d and 5d element nanoclusters that show emergent magnetism, metal–organic structures and surface-supported single molecule magnets, it is desired that interactions with the substrate do not suppress their magnetism.

4.1. Magnetic atoms on nonmagnetic surfaces

4.1.1. Fe and Co impurity atoms on Pt surfaces. The incomplete filling of their electronic d shell results in spin (m_S) and orbital (m_L) moments as in most isolated transition-metal atoms. For Co atoms, for instance, $m_S = m_L = 3\mu_B$, and for Fe atoms, $m_S = 4\mu_B, m_L = 2\mu_B$, as constructed from Hund's rules. In the bulk, those moments are significantly reduced due to electron hybridization and crystal field effects. In particular, the orbital moments per atom are quenched by the interaction of the d orbitals with the crystal field and are as low as $0.15\mu_B$ and $0.1\mu_B$ for Co and Fe, respectively [204]. The magnetic anisotropy is, in the simplest approach, directly related to the anisotropy of the orbital moment and the spin–orbit coupling [192], but more generally on the local atomic environment (see section 3.4).

Magnetic studies on Co adatoms on Pt(111) revealed large orbital magnetic moments per atom, which are increased by over 700% with respect to bulk Co, as well as the giant magnetic anisotropy of approx. 9 meV/atom [74]. Such large values for the orbital moments and the anisotropy are due to the reduced coordination and the electronic hybridization with the substrate. For dimers, trimers and larger clusters of Co, both m_L and the anisotropy energy decrease rapidly with size.

In comparison to that, Fe impurities also exhibit enlarged magnetic moments and anisotropy, but to lesser extent than Co. The smallest Fe nano-islands have been fabricated by deposition of 0.2 ML Fe on Pt(111) at approximately 8 K substrate temperature. At this temperature, the Fe atoms are randomly distributed on the Pt surface, which results in a statistical distribution of the cluster size. The distribution of the cluster size Fe_N was modeled in a simple Monte Carlo simulation, in which negligible mobility of the adatoms was assumed. The results of the simulation, presented in figure 10(b), shows that for nominally deposited 0.2 ML Fe, approx. 64% of the ad-particles are monomers, 83% are monomers and dimers, and 90% and 94% of the ad-particles contain three and four atoms or less, respectively.

Magnetization loops of this sample, obtained with XMCD at 8 K, are shown in figure 10(a) [203]. The difference between the loops, which were taken at angles of $\theta = 0°$ and 65° with respect to the surface normal, reflects the perpendicular magnetic anisotropy of these structures. With the particle size distribution from Monte Carlo simulations, and the magnetic anisotropy as a function of particle size from *ab initio* calculations, the experimental magnetization loops were simulated (lines in figure 10 a). The agreement of the simulations of the magnetization loops for particle ensembles containing monomers, dimers and trimers with the experimental data is remarkable (solid line), since no free

parameters were used. Further improvement was achieved by also including tetramers in the simulation (dashed lines), due to their considerable statistical weight of about 20% [203].

4.1.2. Kondo effect in magnetic impurities on metal substrates. The Kondo effect arises when electrons of a spatially confined magnetic system with discrete energy levels (such as 3d element atoms) interact with the conduction electrons of an otherwise nonmagnetic metal (a metallic matrix or substrate), as has been outlined in section 3.7. Correlated electron exchange processes between the magnetic impurities and the nonmagnetic host effectively flip the spin of the impurity, while simultaneously creating a spin excitation in the Fermi sea of the substrate. The Kondo effect was originally discovered in bulk materials, but also impurity atoms or smallest clusters on nonmagnetic metallic surfaces can exhibit the Kondo effect. The latter represent a model system to study Kondo physics with scanning tunneling microscopy, which is the focus of this section.

The Kondo effect has two profound experimental consequences: (i) the magnetization is reduced below the free-moment value due to the screening and (ii) the electron scattering cross section of the impurity is strongly enhanced, resulting in transport anomalies near and below the Kondo temperature, T_K. The Kondo resonance is experimentally observable on surface-supported magnetic atoms with low-temperature scanning tunneling spectroscopy (STS). It shows up as a Fano resonance near the Fermi energy in the differential conductance of the tunneling contact, dI/dV, at the lateral adatom position. The dI/dV lineshape at the Kondo resonance can be described by the Fano function [205, 206], which includes a lineshape parameter, the position of the Kondo resonance with respect to the Fermi energy and a parameter that is proportional to T_K. The Kondo temperature and the energy of the resonance can thus be determined easily from fits to the dI/dV spectra at the resonance [207].

The dependence of the Kondo parameters of Co adatoms on the substrate material and surface orientation have been comprehensively studied for Co atoms on different substrate surfaces by Wahl *et al* [207]. The experiments show strong dependence of T_K on the substrate material and orientation, and values of T_K ranging from 40 to 90 K were reported. This result is ascribed to the substrate-dependent hybridization of the d levels of the impurities with the neighboring substrate atoms, which determines the level occupation in the substrate and the impurity atoms. Relevant quantities are the number of nearest substrate atoms to the impurity and the spatial extent of the d orbital. It was demonstrated that only the substrate atoms in direct contact with the impurity determine the Kondo temperature. This conclusion is not trivial, since the spatial extent of the Kondo cloud is believed to be as large as several tens or hundreds of nanometers [208].

The Kondo effect can serve as a local probe to determine the exchange interaction in sub-nanometer clusters. For instance, the magnetic ground state of spin-frustrated Cr trimers [6] and the exchange interaction between single Ni or Co atoms [209, 210] could be determined from measurements of the Kondo state the clusters form with the substrate. Recent experiments have demonstrated that the Kondo effect can be manipulated by tuning the interaction with the bulk-state electrons via local coordination, chemical bonding or quantum size effects [211–213]. Potential applications for the Kondo effect may arise in spintronics and quantum information processing. The projection of the Kondo effect with quantum resonators might be exploited to transport information in systems which are too small for conventional wiring [214].

4.1.3. The role of magnetic anisotropy in Kondo systems. As mentioned in the previous paragraph, magnetic anisotropy has a significant effect on the Kondo behavior. For example, easy-axis anisotropy favors spin states with $s_z = \pm s$ ($s \geqslant 1$). Spin-flip processes of conduction electrons, which correspond to $s = 1/2$ or $\Delta m = \pm 1$, are not able to realize the Kondo flipping of the magnetic atoms. In the easy-plane limit, the lowest-lying states of the magnetic atom have $s_z = \pm 1/2$, or $\Delta m = \pm 1$ and undergo Kondo scattering. The relation between Kondo screening and magnetic anisotropy can be studied by measuring the Kondo resonance as a function of applied magnetic fields. However, fields achieved by standard lab magnets are of the order of several tesla (T) and thus orders of magnitude lower in energy than the correlation energy of typical Kondo systems. As a rule of thumb, 1 T $\approx$ 1 K, and typical Kondo temperatures are of the order of several 10–100 K.

This problem was elegantly solved by Otte *et al* by decoupling the magnetic impurities somewhat from the Cu(100) substrate using Cu_2N monolayer islands [215]. For impurities located on such insulating islands, the Kondo temperature is significantly reduced and comparable in energy with magnetic fields of only a few tesla. Spectroscopic measurements with STM on Co impurities situated at specific lattice sites on the Cu_2N islands revealed a splitting of the Kondo peak, which is dependent on the lattice site, and on the magnitude and direction of an applied magnetic field. This anisotropy of the peak splitting was ascribed to the presence of magnetocrystalline anisotropy.

Taken from these studies is that Kondo resonances emerge for large spin impurity atoms only if the magnetic anisotropy creates degenerate ground-state levels (comparable in energy to the characteristic Kondo energy $k_B T_K$) that are connected by the spin flip of a screening electron. Strong magnetic anisotropy can suppress spin-flip transitions, and thus Kondo screening, or influence the Kondo peak split in the presence of magnetic fields.

4.2. Chains and stripes of atoms

In this section, we compare the magnetism of monatomic Co and Fe chains. The fabrication of such chains on Pt(997) has been described in detail in section 2.2.1. XMCD measurements have been performed on Co chains [74, 216] and on Fe chains [8, 60] as a function of coverage, temperature and applied magnetic field. The magnetic XMCD signal is shown in figure 11(b) for Fe and Co chains as a function of the angle of an applied magnetic field of 1 T with respect to the surface normal. The easy magnetization directions are

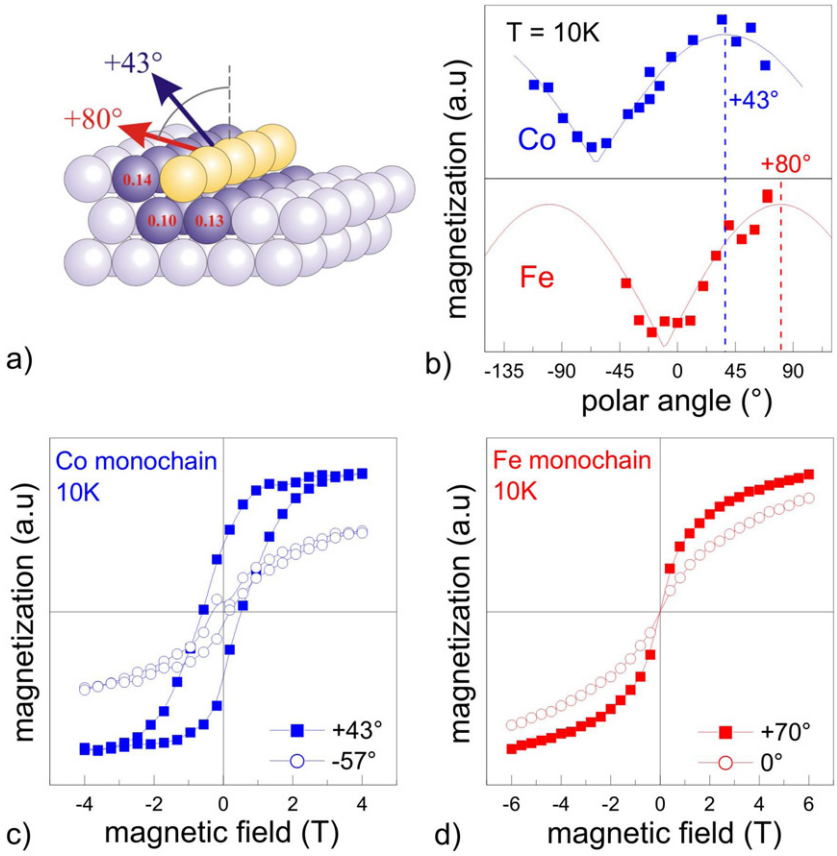

Figure 11. Magnetism of 1D Fe and Co monowires on Pt(997) [216, 94]. (a) Schematic wire orientation. The wires are aligned along the ⟨111⟩ oriented step edges between adjacent (111) terraces of platinum. (b) Non-saturated magnetization of Co and Fe in a magnetic field of 1 T, measured as a function of the angle with respect to the surface normal in a plane perpendicular to the wire axes. ((c) and (d)) Hysteresis loops for Co and Fe wires along the easy and hard magnetization directions.

determined from the maxima of these curves. They are found to be perpendicular to the wire axes, at angles of 43° and 80° to the surface normal in the step-up direction for Co and Fe, respectively.

The magnetocrystalline anisotropy energy (MCA) can be estimated from fits to the magnetization loops taken along the easy and hard magnetization directions in the paramagnetic phase [74]. Values for the MCA of 0.42 meV per Fe atom and 2.0 meV per Co atom in the chains have been determined. Both values are significantly increased with respect to bulk Fe and Co (bcc-Fe: 4 μeV/atom, hcp-Co: 65 μeV/atom). The larger MCA for Co results in ferromagnetic ordering at experimental temperatures of 10 K, observable as open magnetization loops in figure 11(c).

Ab initio calculations suggests similarities in the physics of Co and Fe with regards to exchange splitting, magnetic moments and MCA energies [217–219]. Studies on free and supported Fe chains [220–223], and Co chains [224, 225, 218, 220, 226–230] generally agree in their prediction of strongly increased m_S and m_L relative to those of the bulk and 2D monolayers, as well as enhanced and complex magnetic anisotropy. These variations are attributed to the reduced overlap of the d orbitals in 1D structures, in analogy to the earlier discussed impurity atoms. A detailed investigation of the spin–orbit coupling contributions from Fe and Co, and also the induced magnetization in Pt, showed that the magnetic anisotropy of the Pt-supported Fe wires is dominated by the spin–orbit coupling at the Pt atoms [217]. If this coupling is turned off in the calculations then only a small magnetic anisotropy originating from the spin–orbit coupling at the Fe sites remains. In contrast, the anisotropy for Pt-supported Co wires is due to competing spin–orbit coupling at the Co *and* Pt sites, which are similar in magnitude.

Interesting behavior of the magnetic anisotropy is observed if the Fe or Co coverage is gradually increased. Higher Co coverage results in the formation of stripes of two, three or more atoms in width [216]. The magnetism oscillates in direction from +46° for the monowires to −60° for the bi-chains and −61° for the tetra-chains, and relaxes back towards the film normal for higher coverages [216]. This fluctuation of the easy-axis direction with increasing coverage is accompanied by an overall decrease of the MCA.

Also Fe continues to grow in the step flow mode if the Fe coverage is increased. However, the edge diffusion of the Fe atoms is less efficient, leading to Fe stripes of non-uniform width [8]. Doubling the Fe coverage from 0.12 ML (monochains) to 0.24 ML (bi-atomic chains) decreases the measured average magnetic moment per atom by over a factor of 4 [8]. With further increasing coverage, the average moment increases again to regain values that are similar to those found

for one monolayer of Fe on Pt(111) at the coverage of 0.7 ML Fe [8, 94].

This behavior is due to the interplay of spin–orbit coupling, exchange interaction and induced Pt magnetism. For Fe, the stripe morphology is an additional parameter. STM images show that the width of the Fe stripes is non-uniform, with segments of one, two or three atoms wide present. The MCA depends strongly on the stripe width and the coexistence of segments of different MCA averages out the total moment and reduces the anisotropy to the observed lower value [60].

Whereas the chains at step edges are excellent model systems to study magnetism in 1D, the results cannot be extrapolated to describe the magnetic anisotropy of perimeter atoms in islands of magnetic materials at surfaces. The anisotropy energy of Co islands on Pt(111) was experimentally determined by Rusponi *et al* [54]. A strong out-of-plane anisotropy was found and ascribed to the dominant contribution of the lower-coordinated perimeter Co atoms to the total anisotropy. Experimental proof was obtained by substituting the core atoms of the Co islands with Pt atoms (see section 2.1.2), leaving only the perimeter Co atoms as a monatomic ring around each Pt core. The anisotropy energy for the perimeter atom was measured to be 1 meV, lower than the anisotropy energy found per atom in the 1D Co chains described earlier, but yet by a factor of 20 larger in magnitude than the anisotropy energy per Co atom in the center of such islands. Perimeter atoms are situated in a different chemical and magnetic environment than atoms at a substrate step edge. The atoms in linear chains have only two neighbors of their own species and five substrate atom neighbors, while perimeter atoms in nanostructures and films have, on average, four neighbors of their own species and three substrate atoms underneath. Perimeter atoms are thus strongly exchange-coupled and ferromagnetism can be observed at temperatures as high as 300 K for sub-monolayer islands.

4.3. Two-dimensional structures

4.3.1. Antiferromagnetic and non-collinear magnetic ordering in monolayer thin films. Nanostructures can exhibit spin structures that do not occur naturally in bulk materials, and can thus be studied as model systems for exchange and competing interactions. Of the magnetic transition metals with bcc crystal structure, Fe is the prototype of a ferromagnet, while both Cr and Mn are basically antiferromagnets. This trend reflects the dominance of antiferromagnetic interactions in approximately half-filled 3d bands (section 3.2) and suggests also that Fe is at the border between ferromagnetism and antiferromagnetism. Thus, small perturbations of its crystal lattice or electronic structure can trigger transitions to antiferromagnetism or more complex non-collinear spin structures. A number of experiments and calculations have indeed shown that Fe layers and nanostructures may be low-spin or high-spin ferromagnetic, antiferromagnetic or nonmagnetic, depending on the lattice parameters [231, 26, 28, 232]. At the origin of such a dependence on the local atomic coordination is the exchange interaction of Fe, which shows a strong dependence on the distance between nearest neighbors and can be positive and negative, i.e. favoring ferromagnetic and antiferromagnetic magnetic ordering [233].

Experimentally, magnetic metals can be synthesized in crystal structures other than their bulk equilibrium structure by growing them epitaxially on substrates of different lattice parameters, or simply by reducing their size to free clusters of only a few atoms. Fe, as an example, can be stabilized in the fcc γ phase at room temperature if deposited as an ultrathin film of only a few monolayers thick on Cu(100) or Cu(111) substrates [231, 26]. As free clusters Fe has been reported to have an icosahedral or cubo-octahedral close-packed structure [234].

Antiferromagnetism has been known to occur in films of Fe in the fcc structure at room temperature [235, 236]. More recent studies of Fe on Cu(100) substrates have revealed layered antiferromagnetism in Fe in the thickness range between approximately 4 and 10 monolayers [237–239], but the exact spin alignment and the mechanism leading to it is still under debate [240, 239]. Recent advances in high-resolution magnetic imaging with spin-polarized scanning tunneling microscopy have made the spin alignment in monolayer thin films directly observable [28, 241, 189, 242]. Specifically for Fe on W(100), a two-dimensional antiferromagnetic ground state was imaged with atomic precision and ascribed to the strong hybridization of the Fe with its four nearest W neighbors [28]. This antiferromagnetic ground state does not exist on W(110), demonstrating that the details of the local atomic environment are of critical importance for the type of magnetic ordering.

Besides antiferromagnetism, more complex, non-collinear spin alignment can also occur in low-dimensional structures. This is usually the case for competing exchange, and less often if the exchange interaction competes with the magnetocrystalline anisotropy and the Dzyaloshinskii–Moriya interaction. A simple example of non-collinear spin alignment is a trimer of Cr atoms, shown in figure 1. Here, non-collinear magnetism arises naturally due to the geometric frustration of antiferromagnetic interactions [6]. A more complex nanoscale magnetic structure has been discovered recently on Fe monolayers on Ir(111) [241]. A unit cell of the found magnetic structure contains 15 Fe atoms, of which 7 magnetic moments point in one and 8 moments point in the opposite direction. Deviations from collinearity seem reasonable, since some of the spins are frustrated in the proposed magnetic mosaic structure. First-principles calculations have shown that the hybridization between Fe and the Ir substrate is strong, can destabilize the ferromagnetic state and is thus causing the complex magnetic phase found.

The unique combination of weak exchange interaction and strong DM interaction is at the origin of chiral magnetic ordering in Mn monolayers on W(110) [189]. The adjacent spins within the Mn monolayer are not perfectly antiferromagnetic as in bulk Mn, but slightly canted. This results in spin spirals of specific chirality, with a period λ of approximately 12 nm (figure 12). The experimental observations are consistent with a Dzyaloshinskii–Moriya-driven magnetic configuration, where the DM exchange is sufficiently large and able to compete with the Heisenberg exchange and

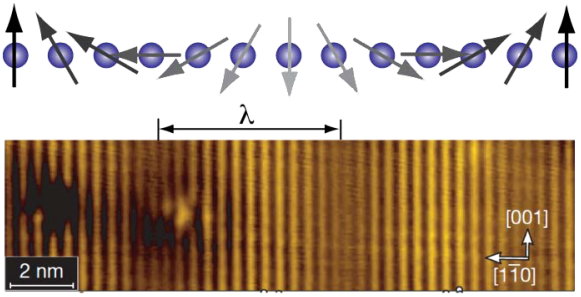

Figure 12. Magnetically resolved STM image of one monolayer of Mn on W(110). The short-period contrast is due to antiferromagnetic alignment of neighboring Mn atoms, while the long-period modulation of wavelength λ is caused by chiral magnetic order. Top: simplified model of one full period of a cycloidal spin spiral which is, among other types of spirals, consistent with the observed spin structure. From [189].

magnetic anisotropy. In fact, for low-dimensional systems that lack inversion symmetry, the exchange interaction, the Dzyaloshinskii vector and the magnetocrystalline anisotropy span a parameter space containing structures with complex spin alignment, including cycloidal, helicoidal and toroidal spin structures and even vortices [243, 189]. Another example where the DM interaction determines the magnetism is the FePt surface alloy is discussed in the following section 4.3.2. These examples show that nanostructures permit us to create and study complex spin structures not present in the bulk by controlling lattice structure and electronic hybridizations, and ultimately competing magnetic interactions, via the substrate.

4.3.2. FePt surface alloys. As discussed, magnetic 3d metals can exhibit large magnetic anisotropies and complex spin alignment, especially Fe, if in contact with heavy 4d and 5d metals. To study such effects in more detail, Fe atoms were embedded directly into the surface of a Pt(997) substrate to form a FePt surface alloy and investigated with STM and XMCD [60]. The details of the synthesis of FePt surface alloys are given in sections 2.1.3 and 2.2.1. The atomically and chemically resolved STM images in figure 13 show a tendency of Fe and Pt to form 2×1 and 2×2 superstructures. The 2×1 structure, consisting of adjacent Fe and Pt rows, is predominantly present near the Pt step edges at low Fe coverages (figure 13 (b)). For higher Fe coverage above 0.5 ML, the atomistic structure of the surface alloy becomes increasingly disordered and contains islands of Fe atoms that are in direct contact with each other (figure 13(a)).

Measurements of the magnetic properties of a $Fe_{50}Pt_{50}$ surface alloy reveal a large out-of-plane magnetic anisotropy of 0.35 meV per Fe atom, as calculated from angular-dependent magnetization loops. Such a large magnetic anisotropy is comparable to that of high-anisotropy bulk-like FePt alloy films, and significantly larger than that of the more dilute $Fe_{25}Pt_{75}$ surface alloy or unalloyed stripes of 0.5 ML Fe. It results in square-shaped magnetization loops with a coercivity of 0.7 T (figure 13(c)).

The key to the large anisotropy in $Fe_{50}Pt_{50}$ surface alloys is the existence of small agglomerates of 5–10 Fe atoms, as identified by *ab initio* calculations [60]. Within these patches, the Fe moments are strongly exchange-coupled ($J \sim 100$ meV/atom), while the rim atoms of such patches are exposed to the strong spin–orbit coupling interaction in the surrounding Pt. This effect is not present in the 2×1 phase. Here, the exchange coupling remains strong within the Fe chains. However, the interchain exchange coupling is only about 1 meV, thereby reducing the total exchange interaction. As a result, Pt-rich $Fe_{35}Pt_{65}$ surface alloys, for example, exhibit only small anisotropy, reflected in reduced coercivity and remanence and thus in *s*-shaped hysteresis loops (figure 13(c)). It is interesting to note that the anisotropy in the surface alloys is so large, even though they do not exhibit the typical tetragonal layered structure that causes large anisotropy in $L1_0$ FePt alloys.

It has been shown theoretically that the Dzyaloshinskii–Moriya interactions (see section 3.5) becomes significant in ideal 2×1 surface alloys, due to the weak interchain exchange coupling [244]. This is predicted to result in non-collinear spin alignment, as shown in figure 14. The q vector has components along and perpendicular to the Fe chains. The wavelength is longer along the chains, which is consistent with stronger exchange in this direction. However, it is interesting to note that the difference in wavelength of the spin spiral in both directions is not more pronounced. It is concluded from the calculations that the anisotropy in spiral systems with q vectors corresponding to several lattice constants is reduced as a result of the averaging of the anisotropy energy due to the particular spin ordering.

4.3.3. Bi/Ag(111) surface alloys. Not really a magnetic system, but strongly influenced by spin–orbit coupling, is the Bi/Ag(111) surface alloy. Generally in a nonmagnetic solid, electronic states of opposite spin orientation are often assumed to be degenerate (Kramers degeneracy), which is a consequence of the time-reversal invariance of electric fields. However, spin degeneracy additionally requires inversion symmetry. In the absence of inversion symmetry, the spin–orbit interaction can actually lift the degeneracy of the electronic states, leading to spin splitting of the electronic states. For bulk crystals that lack a center of inversion symmetry this leads to the so-called Dresselhaus effect. At the surface of a solid where the inversion symmetry is inherently broken, the splitting of surface states can be described by the Rashba–Bychkov model (for a overview see, e.g., [245]), which was originally developed for 2D electron gases in asymmetric semiconductor heterostructures. In particular, clean surfaces of noble metals show spin-split surface states, where the splitting increases with the strength of the atomic spin–orbit coupling. For Au(111) surface states, the Rashba–Bychkov splitting can be described by an energy contribution of the form $\boldsymbol{\sigma} \cdot (\nabla V \times \mathbf{k})$, where $\boldsymbol{\sigma}$ and $\mathbf{k}$ are the spin and momentum operators, and ∇V is the gradient of a potential pointing normal to the surface. Note that this is basically the same expression as in section 3.6, below equation (10). For a free-electron surface state with an effective mass m^* this energy term splits the parabolic spin-up and spin-down bands by $\pm\Delta k$ with respect to the high symmetry point and

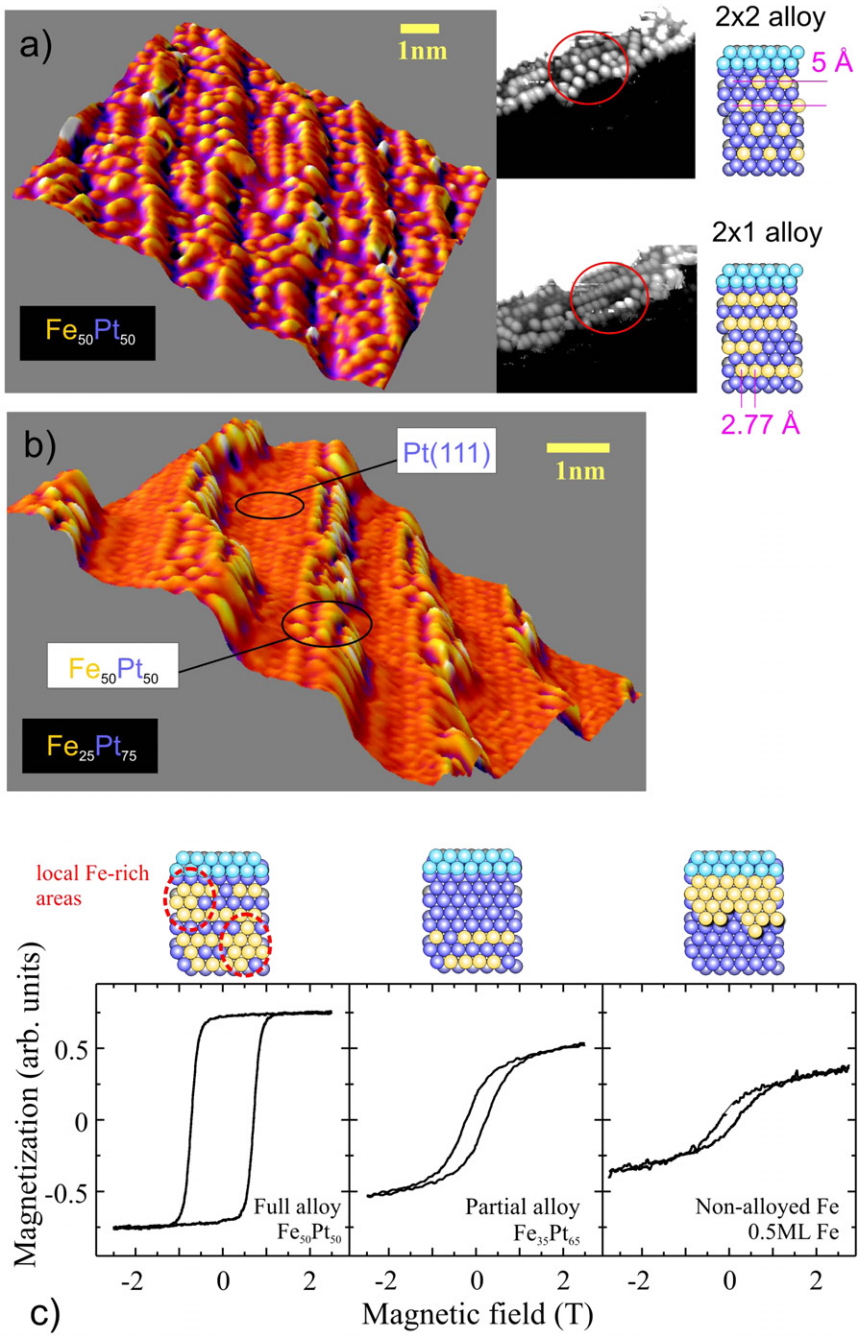

Figure 13. STM images of Fe_xPt_{1-x} surface alloys. (a) $Fe_{50}Pt_{50}$ surface alloy, exhibiting 2×2 and 2×1 superstructures. (b) $Fe_{25}Pt_{75}$, exhibiting the 2×1 superstructure, which formed mainly close to the step edges. (c) Polar magnetization curves for $Fe_{50}Pt_{50}$ and $Fe_{35}Pt_{65}$ surface alloys and for non-alloyed Fe stripes on Pt(997) [60].

leads to an energy dispersion according to $E(\mathbf{k}) = \frac{\hbar^2}{2m^*}(k \pm \Delta k)^2 + E_{SO}$, where E_{SO} is a constant offset due to the k-independent spin–orbit coupling. It should be noted that, although the states are spin-polarized, the surface remains nonmagnetic. A suitable parameter to quantify the Rashba–Bychkov effect is the so-called Rashba energy defined as $E_R = \hbar^2(\Delta k)^2/2m^*$, which describes the effective mass-dependent energy difference between the band extrema and the crossing point at the high symmetry point. According to the definition, the Rashba energy is significant if both the curvature of the parabola and the splitting Δk are large. Interesting here is that the gradient of the potential ∇V, and thus the spin splitting, can be manipulated by the adsorption of adatoms. This is fascinating, as it allows for the use of surface nanostructures to control the spin splitting of two-dimensional electronic states.

A strong spin splitting has been observed in Bi/Ag(111) surface alloys with angle-resolved photoelectron spectroscopy [246]. The deposition of 1/3 of a monolayer of Bi results in the formation of an ordered $(\sqrt{3} \times \sqrt{3})$R30° substitutional $BiAg_2$ surface alloy with threefold symmetry

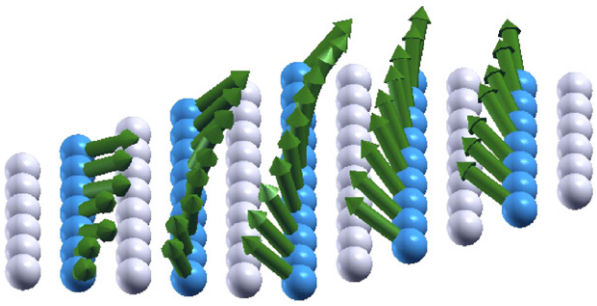

Figure 14. Magnetic structure of a 91-atom 2D FePt (2×1) alloy cluster on a Pt(111) surface from Monte Carlo simulations at $T = 0.1$ K [244]. The arrows denote the orientation of the magnetic moments of the iron atoms.

with an unusually large Rashba energy $E_R \approx 200$ meV in its surface electronic structure. A splitting of such magnitude cannot be explained by the large spin–orbit coupling constant of the heavy element Bi alone: the surface state in Bi(111), for comparison, is split by merely ≈14 meV. Therefore the key to the large Rashba energies in the Bi/Ag(111) surface alloy has to be sought in the structure itself and is presently under debate. One model suggests an outward buckling of Bi atoms of the surface alloy leading to a modification of the potential ∇V [247]. This can cause a strong distortion of the surface wavefunction and a rotation of the spin polarization out of the surface plane. This concept, if confirmed in further studies, could thus potentially lead to a new class of nanoscale materials for spintronic devices with controllable spin-related properties.

4.3.4. Supramolecular control of the magnetic anisotropy. The properties of magnetic metal ions integrated into supramolecular nanostructures are determined by ligand field effects, in contrast to the electronic hybridization in the metallic systems discussed thus far. As an example of the potential of metal–molecule nanostructures in regards to materials design and control of magnetism, we want to discuss the properties of self-assembled two-dimensional (2D) spin arrays containing Fe atoms, which are regularly spaced by 1,4-benzenedicarboxylate molecules (TPA). STM images of such a 2D metal–molecule hybrid layer grown on Cu(100) are shown in figure 15 [248].

Given the spacing of the Fe ions in these networks, exchange interaction between the Fe spins is negligible and the electronic and magnetic properties are determined by ligand field effects. The Fe ions in such networks are thus not comparable to isolated Fe atoms on Cu substrates. The latter constitutes a Kondo system, as described in section 4.1.2, due to the overlap of the Fe 3d and 4s states with the substrate's electronic bands. For the Fe–TPA networks discussed here, the Fe–Cu hybridization is strongly reduced by the square-planar lateral coordination to the TPA molecules, making the coordination of the Fe impurities with the four oxygen atoms of the neighboring TPA molecules the dominant interaction.

XMCD measurements reveal sizable spin moments of the Fe^{2+} in the networks at $T = 8$ K. Magnetization loops taken at the Fe L_3 absorption edge for fields applied within the network plane and perpendicular to the surface show that the easy magnetization direction is within the film plane (figure 15). The origin of this magnetic anisotropy is the spin–orbit interaction-induced mixing of ground and first excited molecular states. The ground-state levels, which have been modeled in a standard multiplet theory as shown in figure 15(c), reflect the square-planar 2D symmetry of the ligand fields by the oxygen atoms. The $d_{x^2-y^2}$ state is highest in energy since its orbital lobes point towards the oxygen atoms. On the other hand, levels pointing partly out of the network plane (d_{xz}, d_{yz} and d_{z^2} states) are found to be lowest in energy. These ground levels mix under the influence of spin–orbit interaction and form the orbital moment with predominant in-plane character, which is the origin of the observed in-plane anisotropy.

To investigate the role of the ligand fields for the magnetic anisotropy of the Fe ions, the magnetism of the Fe–TPA networks has been studied before and after exposure to molecular oxygen under ultrahigh vacuum conditions. The key observation was that the magnetic easy axis reorients from in-plane to out-of-plane as a result of the oxygen adsorption (figure 15(b)). STM images taken after oxygen exposure show the O_2 situated on top of the Fe centers (full circle in the STM image of figure 15(b)). The calculated level diagram for this adsorbate system reflects the changes in the multiplet structure, see figure 15(d). The d_{z^2} level in particular is pushed up in energy due to its susceptibility to coordination in the normal direction. This change in the ligand fields due to O_2 adsorption is strong enough to induce a reorientation of the magnetic easy axis in the normal direction. The supramolecular Fe–TPA network represents thus an interesting model system where the magnetic anisotropy of individual magnetic impurities can be chemically modified.

4.4. Compact surface-supported clusters

Clusters of Fe, Ni or Co atoms in the gas phase show enhanced magnetic moments per atom [19, 249] and their moments and magnetic anisotropy are dependent on the number of atoms [250, 251]. For *surface-supported* clusters the mere size and shape are not the only parameters that determine their properties. Mutual interactions [252], interactions with the substrate [253] or substrate-mediated interactions influence the magnetic and electronic behavior of small clusters, thereby offering a wealth of possibilities for controlled manipulation of such properties by the substrate. Experiments aiming at isolating substrate effects on the cluster properties are reviewed in this section.

4.4.1. Deposited 3d metal nanoclusters. The clusters studied in this section have been formed by buffer-layer-assisted growth, which has been described in section 2.1.4. The advantage of this approach is that clusters form on a Xe film and are thus decoupled from the substrate, before they are brought into contact with the substrate by Xe desorption. STM images and MOKE magnetization loops of an epitaxial film as well as of clusters, formed of nominally deposited 2 ML Fe on Pt(997), are summarized in figure 16. The diameter

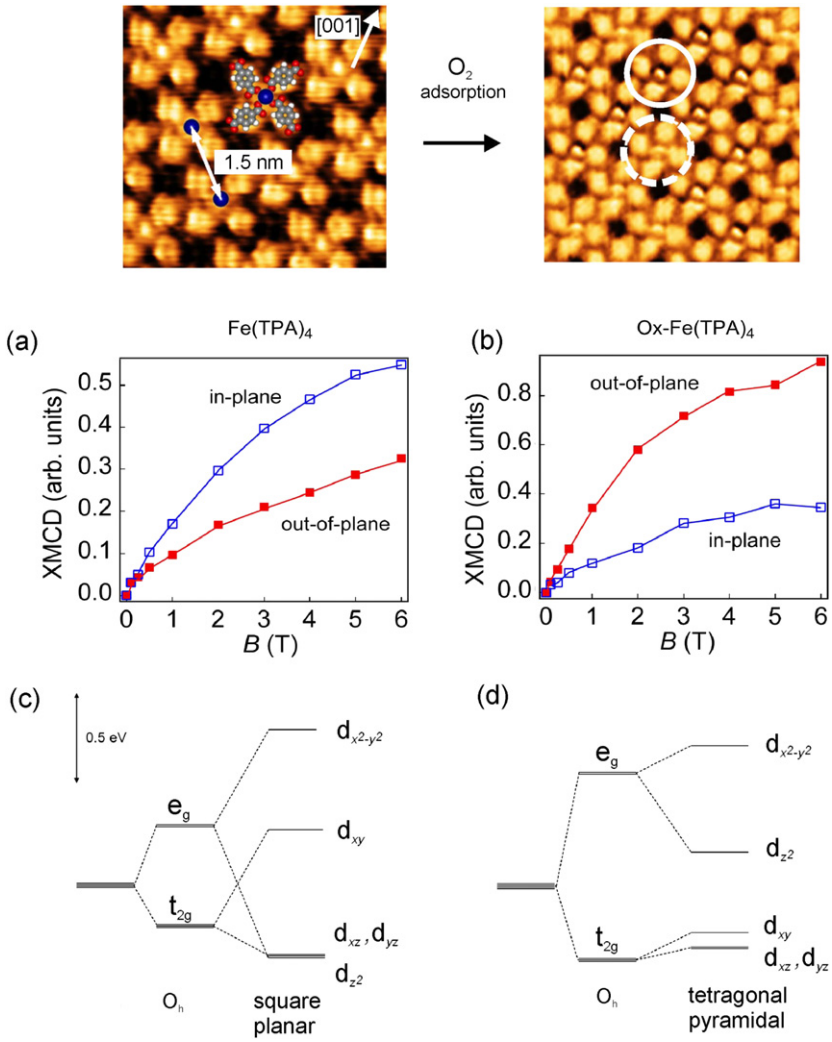

Figure 15. Fe centers within TPA-based molecular networks shown in the STM images. (a) Magnetization curves of $Fe(TPA)_4$ and (b) O_2-$Fe(TPA)_4$ measured at $T = 8$ K in the polar ($\Theta = 0°$, full symbols) and close to in-plane direction ($\Theta = 70°$, open symbols). The magnetic properties are measured by XMCD. (c) Level diagram of $Fe(TPA)_4$. With oxygen adsorption the ground state changes from d_{z^2} towards the degenerate (d_{xz}, d_{yz}) levels (d). The HOMO–LUMO gap changes accordingly.

of the clusters, which appear with flattened hemispherical shapes after making contact with the surface, increases from 2.0 ± 1.0 nm to 9.9 ± 7.6 nm, as the Xe coverage used during BLAG is increased from 5 ML (b) to 45 ML (d). STM tends to overestimate the cluster size due to well-known tip convolution effects, and hence the quoted cluster sizes are an upper limit. Without the Xe layer, the Fe grow as a film in the Volmer–Weber mode at substrate temperatures of 300 K and below [66] (figure 16(a)). Misfit dislocations are formed to reduce the epitaxial stress in the films and are visible as darker lines in the islands of the second and third layers in (a).

The MOKE magnetization loops in figures 16(e)–(h) are taken on samples identical to those in (a)–(d). For the clusters, preferential in-plane magnetization is found, in contrast to the perpendicular anisotropy found for the epitaxial Fe layer. The increase of the average cluster size with Xe buffer layer thickness is reflected in an increases of the total magnetic signal. The loops are not saturated at the maximum available field, as a result of a distribution of the cluster size and orientation.

The observed difference in the magnetic anisotropy between epitaxial films and compact clusters is ascribed to interface contributions to the total magnetic anisotropy energy. Such contributions, arising at the Fe–Pt and Fe–vacuum interfaces, are expected to be more important for the epitaxial film [94]. The reason is the larger volume contribution in clusters, as compared to the flat films. But also the magneto-elastic contributions to the anisotropy energy of Fe is favoring out-of-plane magnetization and in the strained films is sufficiently large to compete with the shape anisotropy [66].

An estimate of the magnetic anisotropy of the clusters can be obtained from measurements of the blocking temperature, as has been shown in [9, 12]. For all cluster samples in figure 16, the magnetic anisotropy is significantly enhanced with respect to bulk Fe and values for the anisotropy energy of $K = 13$ μeV/atom were determined (compare to bulk Fe: 4 μeV/atom) [9, 12]. The anisotropy of the compact clusters is increased due to the Fe–Pt interface contribution, analogous to the impurity atoms discussed earlier. The clusters hybridize with the underlying substrate, thus producing a cloud

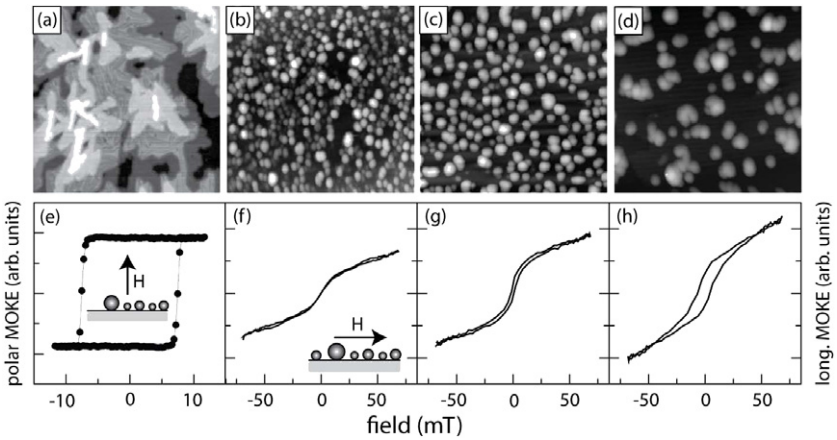

Figure 16. STM images and MOKE hysteresis loops of Fe on Pt substrates. The structures have been synthesized from approx. 2 ML Fe, using 0 ML Xe (a), 5 ML Xe (b), 18 ML Xe (c) and 45 ML Xe (d) as buffer layer during growth. Magnetization loops have been obtained with polar MOKE (e) and longitudinal MOKE ((f)–(h)) under UHV [66, 9].

of magnetic polarization in Pt [249, 254]. Although the contact to the substrate somewhat reduces the average spin moment per atom in the cluster (see also section 4.4.1), it introduces a moment in the d band of the substrate, which might even be extended beyond the region of physical contact [255]. Hence, the effective magnetic volume as well as the anisotropy is increased, which stabilizes the overall magnetization and ties the cluster magnetization to the substrate lattice [31].

The majority of theoretical work agrees that enhanced spin and orbital moments are carried by the outermost shells, and strong deviations of the moment per atom inside the cluster as a function of the atomic sites can be expected [22–24, 256]. Such a significance of the surface atoms makes the magnetism of clusters sensitive to the cluster shape and to any direct contact with substrates or a matrix [252, 253, 257, 258]. To study the role of the substrate for the cluster morphology and magnetism in greater detail, the smallest clusters of Co were prepared next by BLAG on two different substrates, Ag(111) and Pt(111), for direct comparison. The choice of these substrates was inspired by the expectation to find differences in the cluster morphology due to well-known differences in the surface free energy of both surfaces, but also in the cluster magnetism due to the discussed magnetic interface anisotropy. Further, Xe buffer layers were exploited to study the cluster magnetism *before* and *after* they make contact with the metal substrate (see BLAG, section 2.1.4). To this end, variable-temperature STM and XMCD experiments were performed while the clusters were still separated from the metal substrate by the Xe buffer layer during the BLAG process [67].

In this example, Ag and Pt substrates were covered with 1 ML of Xe prior to deposition of 5% of a monolayer of Co. STM images taken on such samples at temperatures between 80 and 300 K reveal significant differences in the buffer-layer-assisted cluster growth on both substrates [67]. On Ag(111), the Co clusters seem to stay atop the Xe until the Xe desorption starts, permitting direct contact of the clusters with the substrate only near the Xe desorption temperature. In contrast, the Co appears to be buried in the Xe on Pt(111) and already in contact with the substrate well below the Xe desorption temperature. After complete Xe desorption, flat Co islands of monolayer height are observed on Pt and compact clusters of semi-hemispherical shape on Ag.

Results from XMCD studies show also differences in the magnetism of the clusters on both substrates before and after Xe desorption. Angular-dependent magnetization loops, taken at the Co L_3 edge as a function of temperature, are summarized in figure 17. For Co on Xe/Ag(111), the magnetization loops are isotropic. A weak in-plane anisotropy becomes visible after Xe desorption. In contrast to that, a pronounced out-of-plane easy axis is observable for the Co clusters on Pt before and after Xe desorption. Remnant magnetization and open hysteresis loops are only found for Co clusters on Pt at temperatures below 10 K.

Quantitative information, such as magnetic anisotropy energy, spin block size or magnetic moments, can again be obtained from the XMCD spectra and from fits to the hysteresis loops in the superparamagnetic regime. The anisotropy energies for Co clusters on Pt are $+0.6$ meV/atom and $+0.67$ meV/atom for Co/Pt before and after Xe desorption. For Co/Ag, we find -0.10 meV/atom. The spin block size is of the order of 15–25 atoms per cluster for all samples shown. The quantitative analysis reflects the well-known trend that the magnetic moments per atom decrease and the anisotropy energies increases as the clusters establish contact with the surface.

The presented studies show that the buffer-layer-assisted growth is dependent on the surface free energies of the cluster material, the buffer layer and the substrate and follows energy considerations described in section 2.1. Cluster synthesis via BLAG is thus not unimpeded by the substrate as previously assumed [61]. However, this finding opens up opportunities to fabricate assemblies of clusters with controlled shape and position using template surfaces, as will be discussed in the following.

4.4.2. Cobalt nanocluster arrays on boron nitride nanomesh templates. Analogous to the experiments presented in the previous section, electronic decoupling of the Co clusters

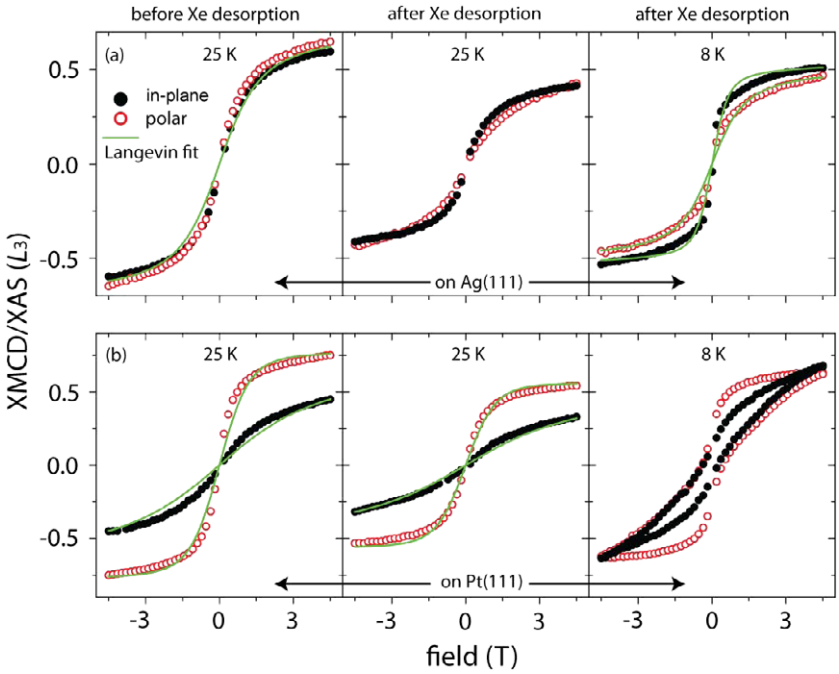

Figure 17. Magnetic XMCD measurements on Co nanoclusters before and after desorption of the Xe buffer layer. (a) 0.05 ML Co on Ag(111) and (b) 0.05 ML Co on Pt(111). The Xe thickness was 1 ML on both substrates. XMCD loops were measured at the temperatures indicated in the panels. The solid lines correspond to Langevin fits according to equation (5) in [203]. The magnetic moment used in the fits are calculated from the XMCD spectra, with $n_h = 2.49$ (Co bulk value) and μ_T derived from *ab initio* calculations [67].

from their substrate can also be achieved by deposition on thin insulator layers. Monolayers of boron nitride, or boron nitride nanomeshes (BN), are ideal to achieve this goal, as they are electrically insulating, chemically inert and mechanically stable, as described in detail in section 2.2.2. The periodically corrugated morphology of the boron nitride layer has been exploited to achieve lateral ordering of deposited metal clusters [70, 71]. The template effect on the cluster growth with BLAG is based on the substrate effects described in the previous section 4.4.1.

Clusters of Co were grown by buffer-layer-assisted growth on boron nitride nanomesh layers. The STM image in figure 18 shows clusters of 1–3 nm in diameter, formed of 15% of a monolayer and 2 ML of Xe. Clearly visible is the lateral ordering of the clusters, which reflects the symmetry of the corrugated nanomesh. A sample like the one shown in the inset of figure 18 has been covered with a metallic overlayer for *ex situ* magnetic characterization with XMCD. The magnetization measurement as a function of applied magnetic field in figure 18 shows a well-known superparamagnetic behavior. Such a behavior is expected for an ensemble of isolated macrospins and can be described with a simple Langevin fit, as shown in the figure. The superparamagnetic behavior of these clusters is in contrast to Co clusters of the same size in contact with a metal substrate, such as Pt (see section 4.4.1). It is concluded that the magnetic anisotropy is very small for this cluster sample due to negligible substrate-induced effects or dipolar interaction. It is further assumed that the crystallographic axes of the clusters are randomized, but this still needs experimental verification.

The possibility to fabricate ordered cluster layers with template substrates could be of technological relevance, for instance for information storage. Clusters of the size achieved in this study would exhibit stable magnetization at room temperature, if fabricated from a typical hard-magnetic material ($K_1 \sim 5$ MJ m^{-3}). The magnetization of smaller clusters would be thermally unstable, whereas larger particles would lead to a waste of space if miniaturization is important [71, 27].

4.5. Emergent magnetism

Emergent magnetism is understood as the onset of magnetic ordering in nanostructures of materials that are nonmagnetic in the bulk, and more generally in any material that is not a traditional d-band magnet. During the last decades, unexpected magnetism has been reported for a variety of materials, including carbon [259], graphene [260], organic monolayers [261, 262], silicon [263–265], Ge [266], PbSe [267], nanocrystals of metals like Au [268–270] and metal oxides, like hafnium oxide and zinc oxide [271–274]. The physical origin of the emergence of magnetism depends on the materials, but is generally linked to defects, doping, surface effects and quantum size effects [275–277, 260, 278].

In this section we will discuss emergent magnetism on the example of Rh nanostructures, with the focus on substrate effects. Free Rh atoms (Rh^+ ions) have a magnetic moment of $\mu_S = 2\mu_B$ and $\mu_L = 3\mu_B$ as a result of the electronic level occupation following Hund's rules. However, magnetic moments are absent in bulk Rh. Experimental studies of gas-phase Rh clusters revealed the emergence of

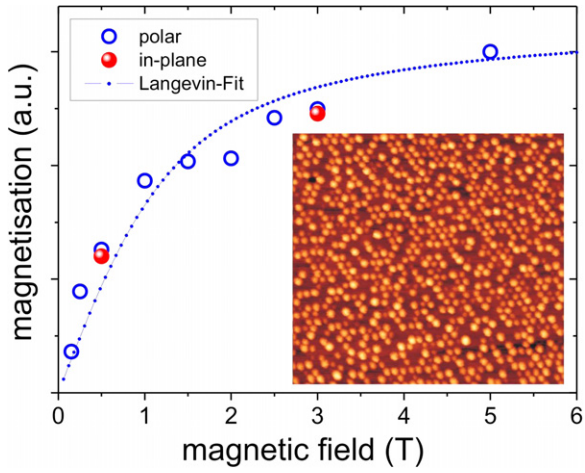

Figure 18. Cobalt cluster arrays on BN shown in the inset were capped with Al_2O_3 and studied using XMCD. The magnetization curves measured in polar and in-plane geometry do not show magnetic anisotropy and can be fitted using a Langevin law.

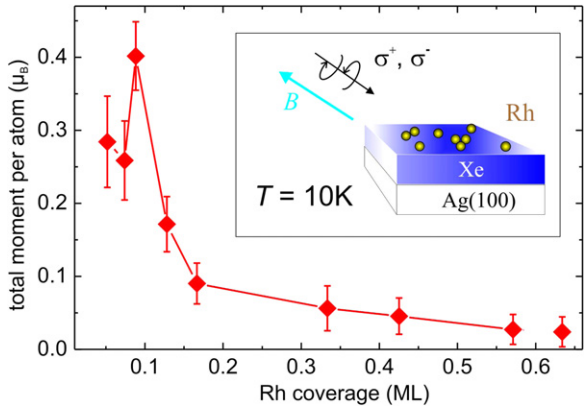

Figure 19. Total moments per Rh atom in clusters on a Xe buffer layer at $T = 10$ K. The moments decay with Rh coverage, due to the increase of the average cluster size. Inset: sketch of the experimental set-up. In the XMCD measurements, positive (σ^+) and negative (σ^-) circularly polarized light was applied in the presence of fields of $B = 5$ T. The lines are guides for the eye.

magnetic moments per atom as the size of the clusters was decreased to below 100 atoms per cluster [279, 20]. This observation has stimulated further experimental and theoretical research addressing the magnetism in 4d and 5d elements. *Ab initio* calculations predicted ferromagnetic ordering for clusters [279] and monolayers [280] of some of the 4d and 5d elements. Experiments revealed a magnetic moment in the surface layer of bulk Rh [20], but interestingly Rh monolayers deposited on several substrates were found to be nonmagnetic [281, 282]. Recent experiments on Rh clusters indicate the existence of a localized magnetic moment in the surface layer of the clusters [281], but small Rh clusters deposited on Ag(100) or Pt(997) did not exhibit magnetism [283]. Despite many of these experiments being quite elaborate and having a substantial error bar, the results nevertheless reflect the known critical dependence of the magnetism in Rh clusters on the exact arrangement of the atoms in the cluster and the bond lengths, the number of atoms per cluster size and the surface orientation of the substrate [278, 284].

Recently, the intrinsic magnetic moment formation was studied on Rh clusters that were in direct contact with Ag(100) and Pt(997) substrates [283] and decoupled from the metal substrate by a thin Xe buffer layer [285]. A sketch of the experimental parameters is given in the inset of figure 19. No net magnetic moment was found for the smallest Rh clusters that have been epitaxially grown on the substrate similar to the approach used for 3d impurities and clusters in section 4.1.1. In contrast, clusters formed with the same amount of Rh by buffer-layer-assisted growth do exhibit net magnetization, as long as they are still decoupled from the metal substrate by the Xe buffer layer. The measured total moment per Rh atom for the Rh clusters on Xe is plotted in figure 19 and it can be seen that the moments decrease with increasing Rh coverage, that is, with increasing cluster size.

Both observations, the decrease of the moment per Rh atom and the vanishing of the moments of the clusters if in contact with the Ag or Pt substrates, are in agreement with the well-known relation between local coordination and magnetic moments (section 3.2). An increased average coordination per Rh atom results in broadened d bands, thereby decreasing the density of states at the Fermi level such that no magnetism is expected according to the Stoner criterion. The increased orbital moments, on the other hand, are related to crystal field effects, that is, the moments are no longer quenched if the cluster size is sufficiently decreased.

The experiments show that it is important for the magnetism in the Rh clusters that they are *decoupled* from the substrate. This observation needs some discussion, since several theoretical studies actually predict emergent magnetism for Rh structures on both Ag and Pt substrates [278]. Several differences between the experimentally and theoretically studied systems exist, which is potentially the reason for the disagreement of the results. (i) The Rh clusters on the Xe buffer layer grow in size when the Xe is desorbed. The clusters that are in contact with the metal substrates are thus larger than the clusters on the Xe, and likely larger than the critical size of ≈100 atoms [285]. (ii) The published calculations in [278, 284] study specific atomic arrangements and cluster sizes, such as pseudomorphic linear chains and related structures. The clusters in the experimental studies are rather compact and structurally relaxed. (iii) Also alloying of the Rh with the substrate atoms cannot be excluded. *Ab initio* calculations actually predict the quenching of orbital and spin moments in alloyed nanostructures [285]. Future experiments must therefore exploit advanced synthesis methods with greater structural control, such as atomic manipulation, to study emergent magnetism in Rh or other nanostructures.

4.6. Single-molecule magnets on surfaces

As the last example of magnetic surface-supported nanostructures that derive their interesting physics because of, or despite, their contact with a supporting substrate, we will

discuss single-molecule magnets (SMM). One of the most widely studied SMMs is a polymetallic manganese complex, commonly called 'Mn_{12}'. SMMs belong to the general class of compounds called exchange-coupled clusters, and collective long-range magnetic ordering of magnetic moments, as in 3d metals, is not present. The most striking feature of SMMs is the quantum tunneling of spins, which is observable in hysteresis loops in the form of a multi-step magnetization reversal [286].

The observation of a magnetic memory effect and the quantum behavior is attractive for applications in information storage and processing. However, this requires us to stabilize the magnetization in SMMs at room temperature, and to attach them on surfaces while at the same time preserving the magnetic properties. These are the current challenges in research on molecular magnets. Deposition of SMMs on surfaces is also desirable for the study with high-resolution scanning probe methods. However, the molecules are often strongly deformed if in contact with substrates, which usually leads to a loss of their intriguing magnetic properties, e.g. their complex magnetic hysteresis.

Evidence that SMMs retain molecular magnetic hysteresis when deposited on metallic surfaces was recently shown for terbium double-decker systems on Cu(111) [15] and Fe_4 complexes on Au(111) [72]. In the latter case using a self-assembly method that started with molecules in solution, the experimentalists deposited a single layer of propeller-shaped molecules, which contains a cluster of four Fe^{3+} ions, onto a surface of gold. While Fe_4 shows simple paramagnetic behavior at $T = 1$ K, open hysteresis loops are observed only at sub-kelvin temperatures. At $T = 0.5$ K the loops took on the typical butterfly shape due to fast magnetization tunneling in zero field, showing unambiguously SMM magnetization reversal. Even though XMCD has recently been used to detect the substrate-driven magnetism of paramagnetic (octaethylporphyrinato)iron(ii) complexes deposited on a ferromagnetic surface [287], this is the first observation of a magnetic hysteresis of purely molecular origin in monolayers.

Despite the very low blocking temperature of Fe_4 and its low remnant magnetization, both consequences of the relatively small spin of this SMM, the results are a first proof of principle that magnetic hysteresis can be observed when SMMs are in contact with a conducting substrate. The importance of this result is evident from the quantum-mechanical origin of magnetic bistability in SMMs: the spin dynamics of SMMs is highly susceptible to geometrical distortions as well as changes in the environment which affect spin–phonon coupling. SMMs are intrinsically fragile systems and previous attempts to demonstrate slow magnetic relaxation in Mn_{12} adsorbates probably failed due to the above given reasons [288].

While the example of Fe_4 is encouraging, the temperatures at which quantum phenomena are observable are far too low to be of technological relevance The results on Fe_4 can therefore only be seen as a proof of principle for fundamental developments in an emerging field of molecular spintronics.

5. Conclusion and outlook

We have outlined some key features of the young scientific discipline of magnetic nanostructures on metallic surfaces, bridging the traditional areas of surface science, molecular physics and nanomagnetism. We discussed the magnetic properties of surface nanostructures on the example of simple self-assembled structures of Fe and Co, such as impurity atoms, chains and clusters. The structures were studied in contact with pristine flat and vicinal surfaces, or decoupled from the substrate by insulating separators. The examples demonstrate how to control atomic coordination, bond lengths and local stoichiometries, and to tune magnetic moments, spin structures, interactions and anisotropies.

The present structures are loosely related to molecular magnets and metal–organic structures, which show interesting magnetic phenomena not observed in pristine metal structures, such as quantum tunneling of the magnetization. The recently discovered graphene [289, 290] has attracted much interest due to interesting and unique properties, such as electronic bands of linear dispersion, leading to zero effective mass for charge carriers [291, 292], bringing about potential applications in spintronics. The magnetism of graphene is caused by imperfections and therefore related to some of the structures discussed here, but graphite-based structures are no metals in a traditional sense and were therefore mentioned only briefly. Magnetic-recording media combine features of both nanostructures on surfaces and granular nanostructures, but were not discussed since a rich review literature on these materials is already available [2, 1, 3].

What can we say about developments in the near and medium future? We are currently learning to control the self-assembly process to advance the complexity of the structures achieved. We envision that further progress in synthesis strategies may lead to complex 2D or even 3D hybrid networks at surfaces, where the functionality of magnetic elements is determined by the matrix they are embedded in. Looking beyond traditional magnetic materials, we anticipate increased research activities on hybrid structures consisting of traditional magnetic nanostructures in contact with metals, polar materials, organics and oxides, to understand and exploit interface effects to control their properties. The presented studies of the effect of embedding into metallic or organic structures have helped setting this trend. Furthermore, we have just begun to manipulate the spin structure with electric fields or with light, and theorists and experimentalists alike have become increasingly aware of the interesting phenomena involved, such as the control of magnetism without a magnetic field.

The discussed synthesis strategies are fairly simple in that they are all based on molecular beam epitaxy. Further progress will depend on improvements of approaches to synthesize structures and materials of unprecedented levels of complexity and with sub-nanometer precision. Simple MBE will be assisted by complementary strategies, such as the deposition from the gas phase, nanolithographic methods and contact printing. Nanostructures themselves can be exploited as templates for the growth of more complex structures and

networks. The synthesis will thus become a multi-step process and depend on the expedient combination of different materials and preparation methods. It is conceivable to build future devices by combining bottom-up with top-down methods, such as from self-assembled functional nanostructures that are connected to the macroscopic world with structures made by lithography [49]. These examples illustrate that research on magnetic surface nanostructures will continue to be fascinating and will offer unprecedented research opportunities in the future.

Acknowledgments

This work has been supported by NSF CAREER (DMR-0747704), NSF MRSEC (DMR-0213808) and DFG (SPP 1153). We would like to thank S Bornemann, X Chen, P Gambardella, H Ebert, K Kern, D A Kunkel, S Mankovsky, J Nitz, G A Rojas, D J Sellmyer, V Sessi, J Zhang and R Zhang for stimulating discussions and collaborative research from which this review has benefited. Parts of figures 1, 2, 3, 11 and 12 are from the literature as cited and reprinted with permission.

References

[1] Weller D and Moser A 1999 *IEEE Trans. Magn.* **35** 4423
[2] Comstock R L 1999 *Introduction to Magnetism and Magnetic Recording* (New York: Wiley)
[3] Weller D and McDaniel T 2006 *Advanced Magnetic Nanostructures* (Berlin: Springer) chapter 11, p 295
[4] Barnas J and Weymann I 2008 *J. Phys.: Condens. Matter* **20** 423202
[5] Santra A K and Goodman D W 2003 *J. Phys.: Condens. Matter* **15** R31–62
[6] Jamneala T, Madhavan V and Crommie M F 2001 *Phys. Rev. Lett.* **87** 256804
[7] Knorr N, Schneider M, Diekhöner L, Wahl P and Kern K 2002 *Phys. Rev. Lett.* **88** 096804
[8] Honolka J *et al* 2009 *Phys. Rev.* B **79** 104430
[9] Zhang J, Repetto D, Sessi V, Honolka J, Enders A and Kern K 2007 *Eur. Phys. J.* D **45** 515–20
[10] Wachowiak A, Wiebe J, Bode M, Pietzsch O, Morgenstern M and Wiesendanger R 2002 *Science* **298** 577–80
[11] Enders A, Repetto D, Peterka D and Kern K 2005 *Phys. Rev.* B **72** 054446
[12] Enders R S A and Sellmyer D 2009 *Nanoscale Magnetic Materials and Applications* (Berlin: Springer)
[13] Bromann K, Felix C, Brune H, Harbich W, Monot R, Buttet J and Kern K 1996 *Science* **274** 956
[14] Shukla N, Ahner J and Weller D 2004 *J. Magn. Magn. Mater.* **272–276** e1349–51
[15] Vitali L, Fabris S, Conte A M, Brink S, Ruben M, Baroni S and Kern K 2008 *Nano Lett.* **8** 3364–8
[16] Rauschenbach S, Vogelgesang R, Malinowski N, Gerlach J, Benyoucef M, Constantini G, Deng Z, Thontasen N and Kern K 2009 *ACS Nano* **3** 2901
[17] Stoner E 1938 *Proc. R. Soc.* A **165** 372–414
[18] Janak J F 1977 *Phys. Rev.* B **16** 255
[19] Billas I M L, Châtelain A and de Heer W A 1994 *Science* **265** 1682
[20] Goldoni A, Baraldi A, Comelli G, Lizzit S and Paolucci G 1999 *Phys. Rev. Lett.* **82** 3156
[21] Wildberger K, Stepanyuk V, Lang P, Zeller R and Dederichs P 1995 *Phys. Rev. Lett.* **75** 509
[22] Guirado-López R, Dorantes-Dávila J and Pastor G 2003 *Phys. Rev. Lett.* **90** 226402
[23] Šipr O, Košuth M and Ebert H 2004 *Phys. Rev.* B **70** 174423
[24] Zhao J, Chen X, Sun Q, Liu F and Wang G 1995 *Phys. Lett.* A **205** 308
[25] Liebermann L, Clinton J, Edwards D and Mathon J 1970 *Phys. Rev. Lett.* **25** 232–5
[26] Shen J, Klaua M, Ohresser P, Jenniches H, Barthel J, Mohan C V and Kirschner J 1997 *Phys. Rev.* B **56** 11134–43
[27] Skomski R, Zhang J, Sessi V, Honolka J, Kern K and Enders A 2008 *J. Appl. Phys.* **103** 07D519
[28] Kubetzka A, Ferriani P, Bode M, Heinze S, Bihlmayer G, von Bergmann K, Pietzsch O, Blügel S and Wiesendanger R 2005 *Phys. Rev. Lett.* **94** 087204
[29] Gambardella P *et al* 2003 *Science* **300** 1130–3
[30] Skomski R and Coey J M D 1999 *Permanent Magnetism* (Bristol: Institute of Physics)
[31] Skomski R 2003 *J. Phys.: Condens. Matter* **15** R841–96
[32] Brune H 2001 Physical properties of thin films and artificial multilayers *Encyclopedia of Materials: Science and Technology* ed K Samwer (Oxford: Pergamon Press) pp 3683–93
[33] Evans J, Thiel P and Bartelt M 2006 *Surf. Sci. Rep.* **61** 1–18
[34] Wuttig M and Liu X 2004 *Springer Tracts in Modern Physics* (Berlin: Springer)
[35] Kotria M, Papanicolaou N I, Vvedensky D D and Wille L T (ed) 2001 *Proc. Nato Advanced Research Workshop on Atomistic Aspects of Epitaxial Growth* (*NATO Science Series. Mathematics, Physics and Chemistry*) vol 65 (Berlin: Springer)
[36] Bauer E 1958 *Z. Kristallogr.* **110** 423
[37] der Merwe J, Woltersdorf J and Jesser W A 1986 *Mater. Sci. Eng.* **81** 1–33
[38] Kunkel R, Poelsema B, Verheij L and Comsa G 1990 *Phys. Rev. Lett.* **65** 733–6
[39] Jenniches H, Klaua M, Höche H and Kirschner J 1996 *Appl. Phys. Lett.* **69** 3339
[40] van der Vegt H A, van Pinxteren H M, Lohmeier M, Vlieg E and Thornton J M C 1992 *Phys. Rev. Lett.* **68** 3335–8
[41] de la Figuera J, Prieto J, Ocal C and Miranda R 1993 *Phys. Rev.* B **47** 13043
[42] Röder H, Brune H, Bucher J-P and Kern K 1993 *Surf. Sci.* **298** 121–6
[43] Elmers H, Hauschild J, Höche H, Gradmann U, Bethge H, Heuer D and Köhler U 1994 *Phys. Rev. Lett.* **73** 898
[44] Sander D, Enders A, Schmidthals C, Reuter D and Kirschner J 1998 *Surf. Sci.* **402–404** 351–5
[45] Berlowitz P, He J-W and Goodman D 1990 *Surf. Sci.* **231** 315–24
[46] Wulfhekel W, Zavaliche F, Bodea S, Hertel R, Steierl G, Liu G, Oepen H and Kirschner J 2003 *Phys. Rev.* B **68** 1444416
[47] Fruchart O, Jubert P, Eleoui M, Cheynis F, Borca B, David P, Santonacci V, Liénard A, Hasegawa M and Meyer C 2007 *J. Phys.: Condens. Matter* **19** 053001
[48] Enders A, Gambardella P and Kern K 2007 *The Handbook of Magnetism and Advanced Magnetic Materials* vol 1 *Fundamentals and Theory* (Chichester: Wiley) chapter (Magnetism of Low-Dimensional Metallic Structures) pp 577–98
[49] Barth J, Costantini G and Kern K 2005 *Nature* **437** 671
[50] Pimpinelli A, Villain J and Wolf D E 1992 *Phys. Rev. Lett.* **69** 985
[51] Enders A, Gambardella P and Kern K 2007 *The Handbook of Magnetism and Advanced Magnetic Materials* vol 1 *Fundamentals and Theory* (Chichester: Wiley)

[52] Brune H, Romainczyk C, Röder H and Kern K 1994 *Nature* **369** 469
[53] Reuter D, Gerth G and Kirschner J 1998 *Phys. Rev.* B **57** 2520
[54] Rusponi S, Cren T, Weiss N, Epple M, Buluschek P, Claude L and Brune H 2003 *Nat. Mater.* **2** 546–51
[55] Röder H, Hahn E, Brune H, Bucher J-P and Kern K 1993 *Nature* **366** 141
[56] Ostwald W 1896 *Lehrbuch Allg. Chem.* 1 **2**
[57] Lee T-Y, Sarbach S, Kuhnke K and Kern K 2006 *Surf. Sci.* **600** 3266–73
[58] Payer D 2001 Diploma thesis *PhD Thesis* Technical University Wien
[59] Schmid M and Varga P 2002 *The Chemical Physics of Solid Surfaces* vol 10 (Amsterdam: Elsevier) chapter (Alloy Surfaces and Surface Alloys) pp 118–51
[60] Honolka J *et al* 2009 *Phys. Rev. Lett.* **102** 067207
[61] Weaver J and Waddill G 1991 *Science* **251** 1444
[62] Huang L, Chey S and Weaver J 1998 *Phys. Rev. Lett.* **80** 4095
[63] Haley C and Weaver J 2002 *Surf. Sci.* **518** 243
[64] Weaver J and Antonov V 2004 *Surf. Sci.* **557** 1–3
[65] Kerner G and Asscher M 2004 *Surf. Sci.* **557** 5
[66] Repetto D, Honolka J, Rusponi S, Brune H, Enders A and Kern K 2006 *Appl. Phys.* A **82** 109
[67] Sessi V, Kuhnke K, Honolka J, Kern K, Enders A, Zhang J, Bencok P, Bornemann S, Minar J and Ebert H 2010 *Phys. Rev.* B **81** 195403
[68] Bansmann J *et al* 2005 *Surf. Sci. Rep.* **56** 189
[69] Shen J, Pierce J, Plummer E and Kirschner J 2003 *J. Phys.: Condens. Matter* **15** R1
[70] Brihuega I, Michaelis C, Zhang J, Bose S, Sessi V, Honolka J, Schneider M, Enders A and Kern K 2008 *Surf. Sci.* **602** L95–9
[71] Zhang J, Sessi V, Michaelis C H, Brihuega I, Honolka J, Kern K, Skomski R, Chen X, Rojas G and Enders A 2008 *Phys. Rev.* B **78** 165430
[72] Mannini M, Pineider F, Sainctavit P, Danieli C, Otero E, Sciancalepore C, Arrio A, cornia A, Gatteschi D and Sessoli R 2009 *Nat. Mater.* **8** 194
[73] Barth J 2007 *Annu. Rev. Phys. Chem.* **58** 375–407
[74] Gambardella P, Dallmeyer A, Maiti K, Malagoli M, Eberhard W, Kern K and Carbone C 2002 *Nature* **416** 302
[75] Bode M, Pascal R and Wiesendanger R 1995 *Surf. Sci.* **344** 185–91
[76] Diaconescu B, Nenchev G, Jones J and Pohl K 2007 *Microsc. Res. Tech.* **70** 547
[77] Corso M, Auwaerter W, Muntwiler M, Tamai A, Greber T and Osterwalder J 2004 *Science* **303** 217
[78] Schiffrin A, Reichert J, Auwärter W, Jahnz G, Pennec Y, Weber-Bargioni A, Stepanyuk V, Niebergall L, Bruno P and Barth J 2008 *Phys. Rev.* B **78** 035424
[79] Stepanyuk V, Negulyaev N, Niebergall L, Longo R and Bruno P 2006 *Phys. Rev. Lett.* **97** 1–4
[80] Li D, Yu C, Pearson J and Bader S 2002 *Phys. Rev.* B **66** 020404(R)
[81] Nötzel R 1996 *Semicond. Sci. Technol.* **11** 1365–79
[82] Brune H, Giovannini M, Bromann K and Kern K 1998 *Nature* **394** 451–3
[83] Temmyo J, Kuramochi E, Kamada H and Tamamura T 1998 *J. Cryst. Growth* **195** 516–23
[84] Tegenkamp C 2009 *J. Phys.: Condens. Matter* **21** 013002
[85] Gambardella P 2003 *J. Phys.: Condens. Matter* **15** S2533
[86] Pratzer M, Elmers H J, Bode M, Pietzsch O, Kubetzka A and Wiesendanger R 2001 *Phys. Rev. Lett.* **87** 127201
[87] Prokop J, Kukunin A and Elmers H 2005 *Phys. Rev. Lett.* **95** 187202
[88] Fujisawa H, Shiraki S, Furukawa M, Ito S, Nakamura T, Muro T, Nantoh M and Kawai M 2007 *Phys. Rev.* B **75** 245423
[89] Ding H, Stepanyuk V, Ignatiev P, Negulyaev N, Niebergall L, Wasniowska W, Gao C, Bruno P and Kirschner J 2007 *Phys. Rev.* B **76** 033409
[90] Pietzsch O, Kubetzka A, Bode M and Wiesendanger R 2000 *Phys. Rev. Lett.* **84** 5212
[91] Gai Z, Farnan G, Pierce J and Shen J 2002 *Appl. Phys. Lett.* **81** 742
[92] Weiss N *et al* 2005 *Phys. Rev. Lett.* **95** 157204
[93] Ehrlich G and Hudda F 1966 *J. Chem. Phys.* **44** 1039
[94] Repetto D *et al* 2006 *Phys. Rev.* B **74** 054408
[95] Gradmann U and Waller G 1982 *Surf. Sci.* **116** 539–48
[96] Brune H, Röder H, Boragno C and Kern K 1994 *Phys. Rev.* B **49** 2997
[97] Schmidthals C, Enders A, Sander D and Kirschner J 1998 *Surf. Sci.* **402–404** 636–40
[98] Hammer L, Meier W, Klein A, Landfried P, Schmidt A and Heinz K 2003 *Phys. Rev. Lett.* **91** 156101
[99] Bachmann M, Gabl M, Deisl C, Memmel N and Bertel E 2008 *Phys. Rev.* B **78** 235410
[100] Negulyaev N, Stepanyuk V, Niebergall L, Bruno P, Auwärter W, Pennec Y, Jahnz G and Barth J 2009 *Phys. Rev.* B **79** 195411
[101] Ma X-D, Bazhanov D, Fruchart O, Yildiz F, Yokoyama T, Przybylski M, Stepanyuk V, Hergert W and Kirschner J 2009 *Phys. Rev. Lett.* **102** 205503
[102] Fruchart O, Klaua M, Barthel J and Kirschner J 1999 *Phys. Rev. Lett.* **83** 2769
[103] Berner S *et al* 2007 *Angew. Chem. Int. Edn* **46** 5115
[104] Laskowski R, Blaha P, Gallauner T and Schwarz K H 2007 *Phys. Rev. Lett.* **98** 106802
[105] Ma H, Brugger T, Berner S, Ding Y, Iannuzzi M, Hutter J, Osterwalder J and Greber T 2010 *ChemPhysChem* **10** 399–403
[106] Preobrajenski A B, Vinogradov A S, Ng M L, Ćavar E E, Westerström R, Mikkelsen A, Lundgren E and Martensson N 2007 *Phys. Rev.* B **75** 245412
[107] Morscher M, Corso M, Greber T and Osterwalder J 2006 *Surf. Sci.* **600** 3280
[108] Corso M, Greber T and Osterwalder J 2005 *Surf. Sci.* **577** L78
[109] Vurens G H, Salmeron M and Somorjai G A 1988 *Surf. Sci.* **201** 129
[110] Nilius N, Rienks E, Rust H-P and Freund H-J 2005 *Phys. Rev. Lett.* **95** 066101
[111] Olsson F, Paavilainen S, Persson M, Repp J and Meyer G 2007 *Phys. Rev. Lett.* **98** 176803
[112] Wegner D and Kaindl G 2009 *Phys. Rev.* B **79** 140406(R)
[113] Land T, Michely T, Behm R, Hemminger J and Comsa G 1992 *Surf. Sci.* **264** 261
[114] Coraux J, N'Diaye A, Engler M, Busse C, Wall D, Buckanie N, zu Heringdorf F-J M, van Gastel R, Poelsema B and Michely T 2009 *New J. Phys.* **11** 023006
[115] Xhie J, Sattler K, Ge M and Venkateswaran N 1993 *Phys. Rev.* B **47** 15835–41
[116] Repp J, Meyer G and Rieder K-H 2004 *Phys. Rev. Lett.* **92** 036803
[117] N'Diaye A T, Bleikamp S, Feibelman P and Michely T 2006 *Phys. Rev. Lett.* **97** 215501
[118] Bogicevic B, Ovesson S, Hyldgaard P, Lundqvist B, Brune H and Jennison D 2000 *Phys. Rev. Lett.* **85** 1910
[119] Morgenstern K and Rieder K-H 2005 *New J. Phys.* **7** 139
[120] Tien J, Terfort A and Whitesides G 1997 *Langmuir* **13** 5349–55
[121] Liu Y, Wang A and Claus R O 1997 *Appl. Phys. Lett.* **71** 2265–7
[122] Gabl M, Bachmann M, Memmel N and Bertel E 2009 *Phys. Rev.* B **79** 153409
[123] Aruga T, Hiroshi T and Yoshitada M 1986 *Surf. Sci.* **175** L725–9

[124] Neugebauer J and Scheffler M 1992 *Phys. Rev.* B **46** 16067
[125] Böhringer M, Morgenstern K, Schneider W-D, Berndt R, Mauri F, Vita A D and Car R 1999 *Phys. Rev. Lett.* **83** 324
[126] Fernandez-Torrente I, Monturet S, Franke K, Fraxedas J, Lorente N and Pascual J 2007 *Phys. Rev. Lett.* **99** 176103
[127] Wegner D, Yamachika R, Wang Y, Brar V, Bartlett B, Long J and Crommie M 2008 *Nano Lett.* **8** 131–5
[128] Rojas G, Chen X, Kim J, Kim J, Dowben P, Xiao J, Gao Y, Zheng Z-C, Choe W and Enders A 2010 *J. Phys. Chem.* C **114** 9408–15
[129] Lee K and Yu J 2005 *Surf. Sci.* **589** 8–18
[130] Stepanyuk V, Negulyaev N N, Niebergall L and Bruno P 2007 *New J. Phys.* **9** 388
[131] Ignatiev P, Negulyaev N, Smirnov A, Niebergall L, Saletsky A and Stepanyuk V 2009 *Phys. Rev.* B **80** 165408
[132] Zhou L, Wiebe J, Lounis S, Vedmedenko E, Meyer F, Blügel S, Dederichs P H and Wiesendanger R 2010 *Nat. Phys.* **6** 187
[133] Repp J, Moresco F, Meyer G, Rieder K, Hyldgaard P and Persson M 2000 *Phys. Rev. Lett.* **85** 2981
[134] Knorr N, Brune H, Epple M, Hirstein A, Schneider M and Kern K 2002 *Phys. Rev.* B **65** 115420
[135] Stepanyuk V, Niebergall L, Baranov A, Hergert W and Bruno P 2006 *Comput. Mater. Sci.* **35** 272
[136] Silly F, Pivetta M, Ternes M, Patthey F, Pelz J and Schneider W 2004 *Phys. Rev. Lett.* **92** 016101
[137] Tsnong T T 1973 *Phys. Rev. Lett.* **31** 1207
[138] Nanayakkara S U, Sykes E, Fernandez-Torres L, Blake M and Weiss P 2007 *Phys. Rev. Lett.* **98** 206108
[139] Negulyaev N, Stepanyuk V, Niebergall L, Bruno P, Hergert W, Repp J, Rieder K-H and Meyer G 2008 *Phys. Rev. Lett.* **101** 226601
[140] Silly F, Pivetta M, Ternes M, Patthey F, Pelz J and Schneider W-D 2004 *New J. Phys.* **6** 16
[141] Stepanyuk V, Baranov A, Tsivlin D, Hergert W, Bruno P, Knorr N, Schneider M and Kern K 2003 *Phys. Rev.* B **68** 205410
[142] Simic-Milosevic V, Heyde M, Nilius N, Nowicki M, Rust H-P and Freund H-J 2007 *Phys. Rev.* B **75** 195416
[143] Stepanyuk V, Niebergall L, LongoSchi R, Hergert W and Bruno P 2004 *Phys. Rev.* B **70** 075414
[144] Liu C, Uchihashi T and Nakayama T 2008 *Phys. Rev. Lett.* **101** 146104
[145] Manai G, Radican K, Delogu F and Shvets I 2008 *Phys. Rev. Lett.* **101** 165701
[146] Stepanyuk V, Negulyaev N, Niebergall L, Longo R and Bruno P 2006 *Phys. Rev. Lett.* **97** 186403
[147] Nilius N, Wallis T and Ho W 2002 *Science* **297** 1853–6
[148] Crommie M, Lutz C and Eigler D 1993 *Science* **262** 218–20
[149] Eigler D and Schweizer E 1990 *Nature* **344** 524
[150] Heinrich A, Lutz C, Gupta J and Eigler D 2002 *Science* **298** 1381–7
[151] Bartels L, Meyer G and Rieder K-H 1997 *Phys. Rev. Lett.* **79** 697–700
[152] Custance O and Morita S 2008 *Science* **319** 1051–2
[153] Tseng A, Notargiacomo A and Chen T 2005 *J. Vac. Sci. Technol.* B **23** 877–94
[154] Hofmann D, Schindler W and Kirschner J 1998 *Appl. Phys. Lett.* **73** 3279
[155] Hu X and von Blanckenhagen P 1999 *Appl. Phys.* A **68** 137–43
[156] Burmeister F, Schäfle C, Matthes T, Böhmisch M, Boneberg J and Leiderer P 1997 *Langmuir* **13** 2983
[157] Kosiorek A, Kandulski W, Glaczynska H and Giersig M 2005 *Small* **1** 439–44
[158] Joe M, Kim J-H, Choi C, Kahng B and Kim J-S 2009 *J. Phys.: Condens. Matter* **21** 224011
[159] Facsko S, Dekorsy T, Koerdt C, Trappe C, Kurz H, Vogt A and Hartnagel H L 1999 *Science* **285** 1551
[160] Slater J C and Koster G F 1954 *Phys. Rev.* **94** 1498–524
[161] Kohn W and Sham L J 1965 *Phys. Rev.* **140** A1133–8
[162] Sutton A P 1993 *Electronic Structure of Materials* (Oxford: Oxford University Press)
[163] Kashyap A, Sabirianov R and Jaswal S S 2006 *Advanced Magnetic Nanostructures* (Berlin: Springer) chapter (Spin-Polarized Electronic Structure) pp 13–39
[164] Jones W and March N H 1973 *Theoretical Solid State Physics I* (New York: Wiley)
[165] Fulde P 1991 *Electron Correlations in Molecules and Solids* (Berlin: Springer)
[166] Schofield A J 1999 *Contemp. Phys.* **40** 95–115
[167] Economou E N 1979 *Green's Functions in Quantum Physics* (Berlin: Springer)
[168] Skomski R 2008 *Simple Models of Magnetism* (Oxford: University Press)
[169] Blundell S 2001 *Magnetism in Condensed Matter* (Oxford: University Press)
[170] Gubanov V A, Liechtenstein A I and Postnikov A V 1992 *Magnetism and the Electronic Structure of Crystals* (Berlin: Springer)
[171] Ising E 1925 *Z. Phys.* **31** 253–8
[172] Shen J, Skomski R, Klaua M, Jenniches H, Manoharan S S and Kirschner J 1997 *Phys. Rev.* B **56** 2340–3
[173] Skomski R and Sellmyer D J 2000 *J. Appl. Phys.* **87** 4756–8
[174] Rau C and Eichner S 1986 *Phys. Rev.* B **34** 6347–50
[175] Skomski R, Waldfried C and Dowben P A 1998 *J. Phys.: Condens. Matter* **10** 5833–8
[176] Arnold C S and Pappas D P 2000 *Phys. Rev. Lett.* **85** 5202–5
[177] Kurz P, Bihlmayer G and Blügel S 2002 *J. Phys.: Condens. Matter* **15** 6353
[178] Yeomans J M 1992 *Statistical Mechanics of Phase Transitions* (Oxford: University Press)
[179] Bander M and Mills D L 1988 *Phys. Rev.* B **38** 12015
[180] Skomski R, Sander D, Shen J and Kirschner J 1997 *J. Appl. Phys.* **81** 4710–2
[181] Bloch F and Gentile G 1931 *Z. Phys.* **70** 395–408
[182] Brooks H 1940 *Phys. Rev.* **58** 909–18
[183] Willoughby S, MacLaren J, Ohkubo T, Jeong S, McHenry M E, Laughlin D, Choi S-J and Kwon S-J 2002 *JAP* **91** 8822–4
[184] Skomski R, Zhang R, Kharel P, Enders A, Liou S-H and Sellmyer D J 2010 *J. Appl. Phys.* **107** 09E126
[185] Dzyaloshinskii I J 1958 *J. Phys. Chem. Solids* **4** 241–55
[186] Moriya T 1960 *Phys. Rev.* **120** 91–8
[187] Skomski R, Kashyap A, Zhou J and Sellmyer D J 2005 *J. Appl. Phys.* **97** 10B302
[188] Skomski R, Honolka J, Bornemann S, Ebert H and Enders A 2009 *J. Appl. Phys.* **105** 07D533
[189] Bode M, Heide M, von Bergmann K, Ferriani P, Heinze S, Bihlmayer G, Kubetzka A, Pietzsch O, Blügel S and Wiesendanger R 2007 *Nature* **447** 190
[190] Dzyaloshinskii I 1965 *Sov. Phys.—JETP* **20** 665
[191] Calvo M R, Fernndez-Rossier J, Palacios J J, Jacob D, Natelson D and Untiedt C 2009 *Nature* **458** 1150–3
[192] Bruno P 1989 *Phys. Rev.* B **39** 865–8
[193] Kang K 2003 *Condensed Matter Theories* (Commack, NY: Nova Science Publishers) chapter (Mesoscopic Kondo Effect) pp 103–10
[194] Chandrasekhar V, Santhanam P, Penebre N A, Webb R A, Vloeberghs H, Haesendonck C V and Bruynseraede Y 1994 *Phys. Rev. Lett.* **72** 2053–6
[195] Thimm W B, Kroha J and von Delft J 1999 *Phys. Rev. Lett.* **82** 2143–6
[196] Újsághy O and Zawadowski A 2005 *J. Phys. Soc. Japan* **74** 80–7
[197] Meissner W and Voigt B 1930 *Ann. Phys.* **399** 761–97
[198] Kondo J 1964 *Prog. Theor. Phys.* **32** 37–49

[199] Ziman J M 1972 *Principles of the Theory of Solids* (Cambridge: University Press)
[200] Bergmann G 1991 *Phys. Rev. Lett.* **67** 2545–8
[201] Krishna-murthy H R, Wilson K G and Wilkins J W 1975 *Phys. Rev. Lett.* **35** 1101–4
[202] Schotte K D and Schotte U 1975 *Phys. Lett.* A **55** 38–40
[203] Bornemann S, Minár J, Staunton J, Honolka J, Enders A, Kern K and Ebert H 2007 *Eur. Phys. J.* D **45** 529
[204] Chen C, Idzerda Y, Lin H-J, Smith N, Meigs G, Chaban E, Ho G, Pellegrin E and Sette F 1995 *Phys. Rev. Lett.* **75** 152
[205] Fano U 1961 *Phys. Rev.* **124** 1866
[206] Újsághy O, Kroha J, Szunyogh L and Zawadowski A 2000 *Phys. Rev. Lett.* **85** 2557
[207] Wahl P, Diekhöner L, Schneider M A, Vitali L, Wittich G and Kern K 2004 *Phys. Rev. Lett.* **93** 176603
[208] Sórensen E and Afflek I 1996 *Phys. Rev.* B **53** 9153
[209] Madhavan V, Jamneala T, Nagaoka K, Chen W, Li J-L, Louie S G and Crommie M 2002 *Phys. Rev.* B **66** 212411
[210] Wahl P, Simon P, Diekhoner L, Stepanyuk V S, Bruno P, Schneider M A and Kern K 2007 *Phys. Rev. Lett.* **98** 056601
[211] Schneider M, Vitali L, Wahl P, Knorr N, Diekhöner L, Wittich G, Vogelgesang M and Kern K 2005 *Appl. Phys.* A **80** 937
[212] Zhao A *et al* 2005 *Science* **309** 1542
[213] Fu Y-S *et al* 2007 *Phys. Rev. Lett.* **99** 256601
[214] Manoharan H C, Lutz C P and Eigler D M 2000 *Nature* **403** 512
[215] Otte A F, Ternes M, von Bergmann K, Loth S, Brune H, Lutz C P, Hirjibehedin C F and Heinrich A 2008 *Nat. Phys.* **4** 847
[216] Gambardella P, Dallmeyer A, Maiti K, Malagoli M, Rusponi S, Ohresser P, Eberhardt W, Carbone C and Kern K 2004 *Phys. Rev. Lett.* **93** 077201
[217] Komelj M, Steiauf D and Fähnle M 2006 *Phys. Rev.* B **73** 134428
[218] Ederer C, Komelj M and Fhnle M 2003 *Phys. Rev.* B **68** 52402
[219] Shick A, Máca F and Oppeneer P 2005 *J. Magn. Magn. Mater.* **290/291** 257
[220] Spiŝák D and Hafner J 2002 *Phys. Rev.* B **65** 235405
[221] Dorantes-Dávila J and Pastor G 1998 *Phys. Rev. Lett.* **81** 208
[222] Lazarovits B, Szunyogh L, Weinberger P and Újfalussy B 2003 *Phys. Rev.* B **68** 024433
[223] Jin Y, Kim I and Lee J 2004 *Phys. Status Solidi* b **241** 1431
[224] Weinert M and Freeman A J 1983 *J. Magn. Magn. Mater.* **38** 23
[225] Komelj M, Ederer C, Davenport J and Fähnle M 2002 *Phys. Rev.* B **66** 140407(R)
[226] Lazarovits B, Szunyogh L and Weinberger P 2003 *Phys. Rev.* B **67** 024415
[227] Shick A, Máca F and Oppeneer P M 2004 *Phys. Rev.* B **69** 212410
[228] Hong J and Wu R Q 2003 *Phys. Rev.* B **67** 020406
[229] Hong J and Wu R Q 2004 *Phys. Rev.* B **70** 060406
[230] Lazarovits U B B, Szunyogh L, Stocks G M and Weinberger P 2004 *Phys. Rev.* B **70** 100404
[231] Kirilyuk A, Giergiel J, Shen J, Straub M and Kirschner J 1996 *Phys. Rev.* B **54** 1050
[232] Cort G, Taylor R and Willis J 1982 *J. Appl. Phys.* **53** 2064–5
[233] Bruno P and Sandratskii L 2005 *Phys. J.* **4** 21
[234] Harris R and McMaster B N 1986 *J. Phys. C: Solid State Phys.* **19** 7217–29
[235] Keune W, Halbauer R, Gonser U, Lauer J and Williamson D L 1977 *J. Magn. Magn. Mater.* **6** 192–5
[236] Halbauer R and Gonser U 1983 *J. Magn. Magn. Mater.* **35** 55–6
[237] Müller S, Bayer P, Reischl C, Heinz K, Feldmann B, Zillgen H and Wuttig M 1995 *Phys. Rev. Lett.* **74** 765
[238] Li D, Freitag M, Pearson J, Qiu Z Q and Bader S D 1994 *Phys. Rev. Lett.* **72** 3112
[239] Qian D, Jin X, Barthel J, Klaua M and Kirschner J 2001 *Phys. Rev. Lett.* **87** 227204
[240] Meyerheim H *et al* 2009 *Phys. Rev. Lett.* **103** 267202
[241] von Bergmann K, Heinze S, Bode M, Vedmedenko E Y, Bihlmayer G, Blügel S and Wiesendanger R 2006 *Phys. Rev. Lett.* **96** 167203
[242] Waśnowska M, Schröder S, Ferriani P and Heinze S 2010 *Phys. Rev.* B **82** 012402
[243] Rößler U, Bogdanov A N and Pfleiderer C 2006 *Nature* **442** 797–801
[244] Mankovsky S, Bornemann S, Minár J, Polesya S, Ebert H, Staunton J and Lichtenstein A I 2009 *Phys. Rev.* B **80** 14422
[245] Petersen L and Hedegárd P 2000 *Surf. Sci.* **459** 49–56
[246] Ast C R, Henk J, Ernst A, Moreschini L, Falub M C, Pacile D, Bruno P, Kern K and Grioni M 2007 *Phys. Rev. Lett.* **98** 186807
[247] Bihlmayer G, Blügel S and Chulkov E 2007 *Phys. Rev.* B **75** 195414
[248] Gambardella P *et al* 2009 *Nat. Mater.* **8** 189
[249] Stepanyuk V S, Hergert W, Wildberger K, Zeller R and Dederichs P H 1996 *Phys. Rev.* B **53** 2121
[250] Pastor G M, Dorantes-Dávila J, Pick S and Dreyssé H 1995 *Phys. Rev. Lett.* **75** 326
[251] Nonas B, Cabria I, Zeller R, Dederichs P H, Huhne T and Ebert H 2001 *Phys. Rev. Lett.* **86** 2146
[252] Lee H K, Schulthess T C, Landau D P, Brown G, Pierce J P, Gai Z, Farnan G A and Shen J 2002 *J. Appl. Phys.* **91** 6926
[253] Pierce J P, Torija M A, Gai Z, Shi J, Schulthess T C, Farnan G A, Wendelken J F, Plummer E W and Shen J 2004 *Phys. Rev. Lett.* **92** 237201
[254] Ederer C, Komelj M and Fähnle M 2003 *Phys. Rev.* B **68** 052402
[255] Garibay-Alonso R and López-Sandoval R 2005 *Solid State Commun.* **134** 503
[256] Aguilera-Granja F, Montejano-Carrizales J and Morán-López J 1998 *Phys. Lett.* A **242** 255
[257] Kechrakos D and Trohidou K 1998 *Phys. Rev.* B **58** 12169
[258] Novosad V, Guslienko K Yu, Shima H, Otani Y, Kim S G, Fukamichi K, Kikuchi N, Kitakami O and Shimada Y 2002 *Phys. Rev.* B **65** 060402
[259] Lüders M, Manini N, Gattari P and Tosatti E 2003 *Eur. Phys. J.* B **35** 57–68
[260] Fernández-Rossier J and Palacios J 2007 *Phys. Rev. Lett.* **99** 177204
[261] Vager Z and Naaman R 2004 *Phys. Rev. Lett.* **92** 087205
[262] Naaman R and Vager Z 2006 *Phys. Chem. Chem. Phys.* **8** 2217–24
[263] Laiho R, Lahderanta E, Vlasenko L, Vlasenko M and Afanasiev M 1993 *J. Lumin.* **57** 197–200
[264] Sheka E, Nikitina E and Zayets V 2003 *Surf. Sci.* **532–535** 754–8
[265] Kopnov G, Vager Z and Naaman R 2007 *Adv. Mater.* **19** 925–8
[266] Liou Y, Lee M and You K 2007 *Appl. Phys. Lett.* **91** 082505
[267] Jian W, Lu W, Fang J, Lan M and Lin J 2006 *J. Appl. Phys.* **99** 08N708
[268] Hori H, Yamamoto Y, Iwamoto T, Miura T, Teranishi T and Miyake M 2004 *Phys. Rev.* B **69** 174411
[269] Crespo P, Litrán R, Rojas T, Multigner M, de la Fuente J, Sánchez-López J, García M, Hernando A, Penadés S and Fernández A 2004 *Phys. Rev. Lett.* **93** 087204
[270] Yamamoto Y, Miura T, Suzuki M, Kawamura N, Miyagawa H, Nakamura T, Kobayashi K, Teranishi T and Hori H 2004 *Phys. Rev. Lett.* **93** 116801
[271] Venkatesan M, Fitzgerald C and Coey J 2004 *Nature* **430** 630
[272] Coey J 2005 *Solid State Sci.* **7** 660–7

[273] Weng H and Dong J 2006 *Phys. Rev.* B **73** 132410
[274] Bibes M and Barthélemy A 2007 *IEEE Trans. Electron Devices.* **54** 1003–23
[275] Ohno H 1998 *Science* **281** 951–6
[276] Dietl T, Ohno H, Matsukura F, Cibert J and Ferrand D 2000 *Science* **287** 1019–22
[277] Luo W, Pennycook S and Pantelides S 2007 *Nano Lett.* **7** 3134–7
[278] Lang P, Stepanyuk V, Wildberger K, Zeller R and Dederichs P 1994 *Solid State Commun.* **92** 755
[279] Cox A, Louderback J, Apsel S and Bloomfield L 1994 *Phys. Rev.* B **49** 12295
[280] Redinger J, Blügel S and Podloucky R 1995 *Phys. Rev.* B **51** 13852
[281] Goldoni A, Baraldi A, Comelli G, Esch F, Larciprete R, Lizzit S and Paolucci G 2000 *Phys. Rev.* B **63** 035405
[282] Chado I, Scheurer F and Bucher J 2001 *Phys. Rev.* B **64** 094410
[283] Honolka J *et al* 2007 *Phys. Rev.* B **76** 144412
[284] Blügel S 1992 *Phys. Rev. Lett.* **68** 851
[285] Honolka J, Sessi V and Kern K 2010 unpublished
[286] Bogani L and Wernsdorfer W 2008 *Nat. Mater.* **7** 179
[287] Wende H *et al* 2007 *Nat. Mater.* **6** 516–20
[288] Gatteschi D, Sessoli R and Villain J 2006 *Molecular Nanomagnets* (Oxford: Oxford University Press)
[289] Novoselov K S, Geim A K, Morozov S V, Jiang D, Zhang Y, Dubonos S V, Grigorieva I V and Firsov A A 2004 *Science* **306** 666–9
[290] Geim A and Novoselov K 2007 *Nat. Mater.* **6** 183
[291] Wallace P 1947 *Phys. Rev.* **71** 622
[292] Charlier J-C, Eklund P, Zhu J and Ferrari A 2008 *Carbon Nanotubes: Advanced Topics in the Synthesis, Structure, Properties and Applications* (Berlin: Springer) chapter (Electron and Phonon Properties of Graphene: Their Relationship with Carbon Nanotubes)